Journal Pre-proofs

Macrophage apoptosis using alendronate in targeted nanoarchaeosomes

Horacio Emanuel Jerez, María Julia Altube, Yamila B. Gándola, Lorena González, Marina Cecilia Gonzalez, María José Morilla, Eder Lilia Romero

PII: S0939-6411(21)00001-1
DOI: https://doi.org/10.1016/j.ejpb.2021.01.001
Reference: EJPB 13494

To appear in: *European Journal of Pharmaceutics and Biopharmaceutics*

Received Date: 8 September 2020
Revised Date: 30 December 2020
Accepted Date: 4 January 2021

Please cite this article as: H. Emanuel Jerez, M. Julia Altube, Y.B. Gándola, L. González, M. Cecilia Gonzalez, M. José Morilla, E. Lilia Romero, Macrophage apoptosis using alendronate in targeted nanoarchaeosomes, *European Journal of Pharmaceutics and Biopharmaceutics* (2021), doi: https://doi.org/10.1016/j.ejpb.2021.01.001

Macrophage apoptosis using alendronate in targeted nanoarchaeosomes

Horacio Emanuel Jerez [1], María Julia Altube[1], Yamila B Gándola[2], Lorena González[2], Marina Cecilia Gonzalez[3], María José Morilla[1] and Eder Lilia Romero[1].

[1]Centro de Investigación y Desarrollo en Nanomedicinas (CIDeN), Universidad Nacional de Quilmes, Bernal, Buenos Aires, Argentina
[2]Universidad de Buenos Aires. Consejo Nacional de Investigaciones Científicas y Técnicas. Instituto de Química y Fisicoquímica Biológicas (IQUIFIB). Facultad de Farmacia y Bioquímica, Buenos Aires, Argentina
[3]INIBIOLP-CONICET, Facultad Cs. Médicas, Universidad Nacional de La Plata, La Plata, Argentina

Abstract

Nanoarchaeosomes are non-hydrolysable nanovesicles made of archaeolipids, naturally functionalised with ligand for scavenger receptor class 1. We hypothesized that nitrogenate bisphosphonate alendronate (ALN) loaded nanoarchaeosomes (nanoarchaeosomes(ALN)) may constitute more efficient macrophage targeted apoptotic inducers than ALN loaded nanoliposomes (nanoliposomes (ALN)). To that aim, ALN was loaded in cholesterol containing (nanoARC-chol(ALN)) or not (nanoARC(ALN)) nanoarchaeosomes. Nanoarchaeosomes(ALN) (220-320 nm sized, ~ -40 mV ξ potential, 38-50 μg ALN/mg lipid ratio) displayed higher structural stability than nanoliposomes(ALN) of matching size and ξ potential, retaining most of ALN against a 1/200 folds dilution. The cytotoxicity of nanoARC(ALN) on J774A.1 cells, resulted >30 folds higher than free ALN and nanoliposomes(ALN) and was reduced by cholesterol in nanoARC-chol(ALN). Devoid of ALN, nanoARC-chol was non-cytotoxic, exhibited pronounced anti-inflammatory activity on J774A1 cells, strongly reducing reactive oxygen species (ROS) and il6 induced by LPS. Nanoarchaeosomes bilayer extensively interacted with serum proteins but resulted refractory to phospholipases. Upon J774A.1 cells uptake, nanoarchaeosomes induced cytoplasmic acid vesicles, reduced the mitochondrial membrane potential by 20-40 % without consuming ATP neither damaging lysosomes and increasing pERK. Refractory to chemoenzymatic attacks, either void or drug loaded, nanoarchaeosomes induced either anti-inflammation or macrophages apoptosis, constituting promising targeted nanovesicles for multiple therapeutic purposes.

Keywords: archaeolipids, endocytosis, apoptosis, inflammation

1. Introduction

The non-metabolizable drug alendronate (monosodium 4-amino-1-hydroxybutylidene bisphosphonate, ALN), is a potent bisphosphonate with high affinity for the bone mineral matrix, highly hydrosoluble [1] and poorly bioavailable by oral route [2]. ALN inhibits the activity of farnesyl diphosphate synthase, a cytosolic enzyme of the mevalonate pathway, impairing the prenylation of small GTPases, critical for macrophages metabolism [3]; it also increases the production of isopentenyl diphosphate, a strong inhibitor of mitochondrial adenine nucleotide translocase [4], inducing apoptotic death of osteoclasts and other macrophages [5]. ALN is administered by oral route as anti-resorptive agent in Paget bone disease, fibrous dysplasia, osteoporosis, myeloma, and to treat bone metastases upon intravenous administration [6]. The *in vivo* activity of ALN on cells other than osteoclasts, however, is underexploited, because of its high affinity for hydroxyapatite, that prevents it from achieving micromolar plasma concentrations on targets other than bone matrix [7].

A general strategy to modify bisphosphonates biodistribution towards extra-bone targets, is loading them in distinct types of nanoparticles. Examples are liposomal clodronate, used to transiently eliminate Kupffer cells [8] and sterically stabilized liposomal ALN, used to eliminate tumour associated macrophages in animal models [9]. Plain liposomal clodronate and liposomal ALN are experimental strategies to transiently reduce circulating monocytes aimed to treat in-stent restenosis [10,11]. Recently however, despite of encouraging preclinical data gathered along nearly 30 years, clinical trials on diabetic patients suffering in stent restenosis and treated with liposomal ALN (BLADE-PCI), have failed [12].

In such frame, and because of the significance of inducing apoptotic death on macrophages other than osteoclasts, the performance of materials alternative to ordinary phospholipids to design improved nanoparticulate drug carriers, is worth to be explored. Archaeolipids for instance, are natural biomaterials of growing market value because of their non-animal (lack of potential viral contamination (i.e. bovine spongiform encephalopathy (BSE)) or vegetal fungal or bacterial origin [13]. Nanovesicles made of archaeolipids receive the generic name of nanoarchaeosomes (nanoARC). Each archaebacteria gender possesses a set of characteristic archaeolipids [14]. NanoARC made of archaeolipids from the hyper halophilic archaebacteria *Halorubrum tebenquichense* are rich in archaeol analogue of methyl ester of phosphatidylglycerophosphate (PGP-Me), a SRA1 ligand [15] and are extensively endocytosed by cells expressing scavenger receptor class A1 (SRA1), such as monocytes, macrophages, neutrophils, immature dendritic and endothelial cells. SRA1 mediated internalization lacks negative feedback [16]; internalised nanoARC thus, are efficacious agents for targeted massive intracellular delivery of carried drugs. NanoARC bilayer, besides of lacking insaturations and being rich in methyl groups perpendicular to the longitudinal chain axe, traps and partition labile or poorly soluble drugs within its structure. Once endocytosed, different types of nanoarchaeosomes (pH-sensitive [15] and ultradeformable nanoARC [17] and ultra-small solid archaeolipid nanoparticles [18]) are used as activity magnifiers upon massive drug delivery to the endo-lysosomal system or cell cytoplasm [19,20]. Thus, we speculate that the ability of ALN and of liposomal (ALN), to induce apoptotic death to macrophages [21], could be improved by naturally targeted nanoarchaeosomes of high structural stability, lack of immunogenicity [22] and drugs trapping ability. Because of that, this work is aimed to screen the effect of nanoarchaeosomes loaded with ALN (nanoARC(ALN)) and nanoARC-chol(ALN) on J774A.1 cell line as model of macrophage. In addition, despite of the undeniable impact that nanoparticles internalization may have on cell homeostasis, the effect of lipids on key cell life events, has been historically poorly addressed. Hence for the first time, lysosomal integrity, mitochondrial activity, mitophagy and signalling proteins upon nanoarchaeosomes internalization were surveyed. The same as nanoliposomes, nanoarchaeosomes are sealed vesicles, but archaeolipids strongly differ from ordinary phospholipids in their interaction with blood proteins, vital cell organoids and signalling pathways, constituting new biomaterials of potential high aggregate value.

2. Materials and methods

2.1 Materials

Soybean phosphatidylcholine (SPC, purity >90%) was a gift from Lipoid (Ludwigshafen, Germany). Hydrogenated soy phosphatidylcholine (HSPC) and distearoyl phosphatidylglycerol (DSPG) were from Northern Lipids Inc. (BC, Canada). Alendronate sodium trihydrate was a gift of Gador S.A. (BA, Argentina). Oil Red O, 6-Dodecanoyl-N,N-dimethyl-2-naphthylamine (Laurdan), 3-(4,5-dimethylthiazol-2-yl)-2,5-diphenyl tetrazolium bromide (MTT), bovine serum

albumin (BSA), Sephadex G-50, propidium iodide (PI), lipopolysaccharides from *Escherichia coli* 0111:B4 (LPS), Mitochondria Staining Kit (JC-1 dye), Trizma base, HEPES, Tween20, Triton X-100, sodium dodecyl sulphate (SDS), glycine, ammonium persulfate, aprotinin, phenylmethylsulfonylfluoride (PMSF), sodium orthovanadate, 2-mercaptoethanol and BSA-fraction V were obtained from Sigma-Aldrich (St. Louis, MO, USA). Cholesterol was from ICN Biomedicals. Lissamine™ rhodamine B 1,2-dihexadecanoyl-sn-glycero-3-phosphoethanolamine triethylammonium salt (RhPE), YO-PRO™-1, CM-H2DCFDA (General Oxidative Stress Indicator), LysoTracker ™ Red DND-99, LysoTracker™ Green DND-26 and MitoTracker™ Red CMXRos were purchased from Thermo Fisher Scientific (MA, USA). PVDF membranes, high performance chemiluminescence film, and enhanced chemiluminescence (ECL) Plus are from Amersham Biosciences (GE Healthcare, Piscataway, NY, USA). Acrylamide, bis-acrylamide, and TEMED were obtained from Bio-Rad Laboratories (Hercules, CA, USA). Antibodies against AKT, phosphor-AKT, p44/42 MAP kinase (ERK1/2), and phospho-p44/42 MAP kinase Thr202/Tyr204 were from Cell Signalling Technology Inc. (Beverly, MA, USA). Antibodies against actin, and HRP-conjugated secondary antibodies were purchased from Santa Cruz Biotechnology Laboratories (Santa Cruz, CA, USA). Roswell Park Memorial Institute 1640 medium (RPMI), penicillin-streptomycin sulphate, L-glutamine and trypsin/ ethylenediamine tetra acetic acid were from Gibco®, Life Technologies (NY, USA). Fetal bovine serum (FBS) was from Internegocios S.A. (BA, Argentina). Yeast extract, Griess Reagent Solution "A" and Griess Reagent Solution "B" were from Laboratorios Britania S.A. (BA, Argentina). The other reagents were of analytic grade from Anedra, Research AG (BA, Argentina).

2.2 Archaebacteria growth and archaeolipids extraction

The extreme halophile *Halorubrum tebenquichense* archaea, isolated from soil samples of Salina Chica, Peninsula de Valdés, Chubut, Argentina were grown in basal medium supplemented with yeast extract and glucose [23]. Biomass was grown in 16.5 L medium in a 25 L homemade stainless-steel bioreactor at 40°C and harvested after 72 h growth. Total polar archaeolipids (TPA) were extracted from biomass using the Bligh and Dyer method modified for extreme halophiles [24]. Around 700 mg TPA were isolated from each culture batch. The reproducibility of each TPA-extract composition was routinely screened by phosphate content [25] and electrospray-ionization mass spectrometry [17].

2.3 Preparation of nanovesicles

Conventional nanoliposomes made of HSPC:cholesterol 7.5:2.5 w:w (HSPC-chol), nanoarchaeosomes made of TPA (nanoARC) and of TPA:cholesterol 7:3 w:w (nanoARC-chol), were prepared by the film hydration method, as described in [19]. Briefly, mixtures of lipids were dissolved in chloroform: methanol 1:1 v:v; solvents were rotary evaporated until elimination The lipid films were flushed with N_2 and hydrated with Tris buffer (10 mM Tris-HCl buffer pH 7.4 with NaCl 0.9 % w:w) up to a final concentration of 10 mg/ml total lipids at room temperature for nanoarchaeosomes and 60ºC for HSPC-chol. The suspensions were sonicated 1 hour with a bath-type sonicator 80 W, 80 KHz and extruded 10-15 times through a sandwich of 0.4 µm and 0.2 µm pore size poly-carbonate filters using a Thermobarrel Extruder (Northern Lipids, Inc. BC, Canada). The resulting nanovesicles were sterilized by passage through a 0.22 µm sterile filter, and stored at 4°C.

To prepare alendronate (ALN) containing nanovesicles (nanoARC(ALN), nanoARC-chol(ALN), HSPC-chol(ALN) lipid films were hydrated with 14 mg/ml of ALN in Tris buffer. Free ALN was removed by gel filtration on Sephadex G-50 using the mini-column centrifugation technique [26]. Briefly, aliquots of 300 µl of nanovesicles were seeded on a 3-ml syringe filled with Sephadex G-50 and centrifuged during 5 min at 700 x g and the first fraction of 240–300 µl was collected.

To prepare RhPE labelled nanovesicles, RhPE at 0.4 µg per mg of lipids was added to the mixture of lipids and lipid films were hydrated with Tris buffer as stated above. RhPE was quantified by spectrofluorometry (λ_{ex} 561 nm and λ_{em} 580 nm) with a LS55 Fluorescence Spectrometer (PerkinElmer Inc. MA, USA), upon complete disruption of 1 volume of nanovesicles in 10 volumes of methanol. The fluorescence intensity of the sample was compared with a standard curve prepared with RhPE in methanol. The standard curve was linear in the range 0.075–0.5 µg/mL RhPE.

In the following sections, the general term nanoarchaeosomes will be used to indistinctly mention nanoARC, nanoARC(ALN), nanoARC-chol or nanoARC-chol(ALN).

2.4 Structural characterization of nanovesicles

Phospholipids content and loaded ALN were quantified by the colorimetric phosphate microassay [25] after extraction of ALN from phospholipids using the Bligh and Dyer method

[27]. ALN was quantified in the aqueous phase while phospholipids were quantified in the chloroform phase.

Size and ζ potential of nanovesicles were determined by dynamic light scattering and phase analysis light scattering, respectively, using a Zetasizer Nano ZS equipment (Malvern Instruments Ltd, UK).

The order and fluidity of nanovesicles were assessed by determining Laurdan generalized polarization (GP) and fluorescence anisotropy (FA) respectively, using a LS55 Fluorescence Spectrometer. Nanovesicles were labelled with Laurdan 1:500 (for GP) or 1:20 (for FA) Laurdan:lipids mol:mol ratio in Tris buffer and were incubated at room temperature for 30 min.

GP was calculated using the following equation:

$GP= (I_{440} – I_{490}) / (I_{440} + I_{490})$

Where I_{440} and I_{490} are the fluorescence intensities at λ_{em} =440 nm and λ_{em} =490 nm respectively and obtained from the spectra between 400-520 nm at λ_{ex} =364nm ($Slit_{ex}$:5.0 nm and $Slit_{em}$: 10.0 nm. Scan Speed: 100 nm/min).

FA was calculated by the fluorimeter software according to the following equation:

$FA= (I_0\text{-}G\ I_{90})/ (I_0+2G\ I_{90})$

Where I_0 and I_{90} are the fluorescence intensities at λ_{em}=440 nm with λ_{ex} = 364 nm and the excitation polarizer oriented at 0° and 90° respectively. The correction factor (G) was obtained from the ratio of emission intensity at 0° and 90° with the excitation polarizer oriented at 90° (after subtraction of scattered light).

Nanovesicles morphology was screened by cryo-electron microscopy (cryo-EM). Lacey Carbon Type A 300 mesh copper grids (Ted Pella, Inc. CA, USA) were submitted to a glow discharge procedure in a PELCO easiGlow™ Glow Discharge Cleaning System (Ted Pella, Inc. CA, USA) (15 mA for 10 seconds), in order to increase their hydrophilicity. The grids were then inserted in a Vitrobot Mark IV System (Thermo Fischer Scientific, MA, USA) where 3 µl of samples were added, and 20 s were given for sample fixation. Subsequently, an automatic blotting (blot force=-5, blot total=3) was performed to dry the excess of sample. Finally, the grid was rapidly plunged into liquid ethane wrapped into a liquid nitrogen environment. Measurements were made in a Talos™ F200C (Thermo Fischer Scientific, MA, USA) microscope at 200 kV with a Ceta™ 16M 4Kx4K CMOS sensor camera (Thermo Fischer Scientific, MA, USA). Sample preparation and data acquisition were performed at the National Laboratory of Nanotechnology (LNNano) at CNPEM - Campinas, São Paulo, Brazil. ImageJ software (National Institutes of Health) was used to image manipulation[28,29].

Adsorption of human serum proteins on nanoARC bilayer in dynamic conditions was determined by Multi-Parametric Surface Plasmon Resonance (MP-SPR) in a SPR-Navi 210A equip from BioNavis (INIFTA-La Plata), with SPR102 AU sensors. Nanovesicles were immobilised on the surface of Au sensor and serum proteins and PLA2 were sequentially injected. The experiment was carried out by duplicate, according to the following scheme: *1) polymer layers adsorption:* first, the sensor Au surface was modified with a layer by layer polymer assembly. A polymer layer was formed while flowing at 15 µl/min, optimizing the adsorption times for each polymer. First the Au substrate was covered with 1 mg/ml polyethyleneimine (PEI) in 10 mM KCl along 15 min, then with 1 mg/ml sodium polystyrene sulfonate (PSS) in 10 mM KCl along 10 min, and finally with 1 mg/ml poly(diallyl dimethylammonium chloride (PDADMAC) in 10 mM KCl along 6 min washing between polymers with 10 mM KCl; as a result, the Au surface was covered with 3 layers: PEI/PSS/PDADMAC. *2) nanovesicles attachment*: suspensions of nanovesicles [nanoARC and nanoliposomes made of SPC:DSPG:chol (4:4:2 w:w) as state in 2.3 section of -36 mV ζ potential, ~ 200 nm Z- Average, PDI 0.2-0.3] at 3 mg total lipids /ml in Tris buffer, were injected in parallel on the PEI/PSS/PDADMAC assembly after a baseline with Tris buffer was obtained. *3) serum proteins injection:* Human serum [from healthy anonymous donors free from HIV, b and c hepatitis and syphilis certified by the Public Health Laboratory from the Exact Sciences Faculty from the National University of La Plata. Total proteins were quantified employing a micro Bicinchoninic acid (BCA) Protein Assay Kit from Thermo Fisher Scientific (Rockford, IL, USA), and diluted in Tris buffer] at 5 mg/ml was injected. *4) phospholipase A2 (PLA2) injection:* a PLA2 solution provided by EnzChek® Phospholipase A2 Assay Kit (Invitrogen) of 500 U.I. /ml (370 µg/ml), at 5 µg/ml in a final volume of 3 ml of Tris buffer, was employed. Nanovesicles and proteins injections were performed along 25 min at a flow speed of 10 µl/min to maximize the contact between surfaces. Between injections the surfaces were washed for 15 min with buffer to remove unspecific bonding. Measurements were carried out at λ 785 nm and 23°C.

2.5 Structural stability of ALN loaded nanovesicles upon dilution

The structural stability of nanoARC(ALN), nanoARC-chol(ALN) and HSPC-chol(ALN) against dilution was determined by dialysis. Briefly, one volume of nanovesicles was dialysed along 3 h employing 12.000 MWCO (Sigma-Aldrich, MO, USA) dialysis activated membranes at 37ºC and 80 rpm against 200 volumes of 20 mg/ml BSA in Tris buffer. Phospholipids and ALN content, size, PDI and ζ potential of samples within the bags were determined as previously described.

2.6 J774A.1 cells growth

Immortalized murine Balb/c macrophages J774A.1 (ATCC® TIB-67™, nearly 20 passages) supplied by Dr Erina Petrera (Facultad de Ciencias Exactas y Naturales, Universidad de Buenos Aires, Argentina) were maintained in RPMI supplemented with 10% FBS, 100 U/ml penicillin, 100 µg/ml streptomycin and 2 mM L-glutamine (complete RPMI medium) in a humidified atmosphere of 5% CO_2 at 37°C. J774A.1 cells express SRA1 [30,31] and constitute a suitable model of macrophages present in atherosclerotic lesions and in inflamed environments.

2.7 Nanoarchaeosomes cytotoxicity

The viability of J774A.1 cells upon 24 h and 48 h incubation with devoid and ALN-loaded nanovesicles was measured by the MTT assay. Briefly, J774A.1 cells were seeded in 96-well plates at a density of 3×10^4 cells per well and grown for 24 h. Then, cells were incubated with nanovesicles at 10, 50, 100 and 500 µg/ml total lipid (TL) or ALN. After 24 h or 48 h of incubation the medium was removed, cells were washed with PBS and 100 µl of 0.5 mg/ml MTT solution was added to each well. After 3 h of incubation, the MTT solution was removed, the insoluble formazan crystals were dissolved in dimethyl sulfoxide, and absorbance was measured at 570 nm in a Cytation 5 Cell Imaging Multi-Mode Reader (Biotek Instruments, VT, USA) (Cytation 5 instrument). The cell viability was expressed as a percentage of the cell grown in medium.

2.8 Nanoarchaeosomes uptake

The uptake of RhPE-nanovesicles by J774A.1 cells was measured by flow cytometry. Briefly, J774A.1 cells were seeded on 24-wells plates at a density of 1.5×10^5 cells per well and grown for 24 h. Then, cells were incubated with 100 µg/ml RhPE-nanovesicles in RPMI supplemented with 5% FBS along 1 and 5 h at 37°C. After incubation, the cells were trypsinized, washed with PBS and a total of 1×10^4 cells were analysed by flow cytometry in a BD FACSCalibur™ (BD Biosciences, NJ, USA) equipment (FACS instrument). The red fluorescence detected at the FL-3 channel was analysed and further normalized to RhPE/total lipid ratio of each formulation. Data were analysed using Flowing Software 2.5.1 (Flowing Software, Finland).

Human plasma (HP) from healthy volunteers' blood was collected by venous puncture in tubes containing heparin (50 IU / ml of blood) as an anticoagulant. The plasma was recovered by centrifugation at 3,000 g for 15 min at 15 °C. The plasma supernatant was divided into aliquots and stored at -80°C. Rho-PE labelled samples were incubated at a concentration of 2.5 mg/ml at a 1:1 nanovesicles: HP v:v ratio at 37 °C for 1 h in an orbital shaker at 200 rpm. Then nanovesicles uptake were measured as stated above using culture medium without FBS.

2.9 Induction of acidic vesicles

The induction of acidic vesicles after nanovesicles uptake by J774A.1 cells was tracked with the fluorescent acidotropic probe LysoTracker ™ Red DND-99 (LR). Briefly, J774A.1 cells were seeded on 24-wells plates at a density of 1.5×10^5 cells per well and grown for 24 h. Then, cells were incubated with 100 µg/ml of nanovesicles in RPMI with 5% FBS along 24 h. After incubation, supernatants were discarded, cells were washed with PBS and incubated with 200 nM LR along 15 min at 37ºC. Afterwards, cells were trypsinized, washed with PBS and a total of 2×10^4 cells were analysed by flow cytometry in a FACS instrument employing a 488 nm laser excitation and collecting the fluorescence in the FL-3 channel. A negative control of RPMI with 5% FBS was used to analyse changes in fluorescence intensity. To assess for reversibility of induction of acidic vesicles, the incubation with nanovesicles was repeated in identical conditions described above, excepting that upon 24 h incubation, the supernatants were discarded, the cells washed with PBS and incubated with RPMI supplemented with 5% FBS along other 24 h. After that, cells were stained with LR and processed as state above.

2.10 Mitochondrial membrane potential (MMP)

The effect of nanovesicles on mitochondrial membrane potential (MMP) of J774A.1 was determined using JC-1 dye according to the manufacturer guidelines. Briefly, J774A.1 cells were seeded in 96-wells plates at a density of 3×10^4 cells per well and growth for 24 h. Then, cells were incubated with nanovesicles as state in 2.9. After incubation, supernatants were

discarded, cells were washed with PBS and incubated with 2.5 µg/ml JC-1 staining mixture along 15 min at 37ºC. Upon supernatant removal and PBS washing, the fluorescence intensity of each well was measured in Cytation 5 instrument. The fluorescence of JC-1 monomers was determined at λ_{ex} 490/10 nm and λ_{em} 530/20 nm and JC-1 aggregates at λ_{ex} 525/20 nm and λ_{em} 590/20 nm. A positive control was carried out by incubating cells with 100 ng/ml Valinomycin.

To assess for reversibility of MMP changes, the incubation with nanovesicles was repeated in identical conditions described above, excepting that upon 24 h, the supernatants were discarded, the cells washed with PBS and incubated with RPMI supplemented with 5% FBS along other 24 h. After that, the MMP was determined as previously explained.

2.11 Mitophagy

The co-localization of mitochondria with lysosomes as mitophagy indicator were determined in J774A.1 cells according to [32]. Briefly, J774A.1 cells were seeded on sterile coverslips in 24-wells plates at a density of 6 × 10^4 cells per well and incubated with nanovesicles as state in 2.9. After incubation, supernatants were discarded, and the cells were co-incubated with the fluorescent dyes LysoTracker™ Green DND-26 (LG) 1µM and MitoTracker™ Red CMXRos (MR) 200 nM at 37ºC along 20 min. After fixing the cells with formaldehyde 4%, the images were acquired by confocal microscopy with a Leica TCS SP8 DLS (Leica Microsystems, Germany). The open source image analysis software (ImageJ, NIH) was used to analyse co-localization.

2.12 Intracellular ATP content

The intracellular ATP content of J774A.1 cells upon incubation with nanovesicles was determined with CellTiter-Glo® Luminescent Cell Viability Assay (Promega, WI, USA) according to manufacturer guidelines. Briefly, J774A.1 cells were seeded and incubated with nanovesicles as state in 2.10. After that, supernatants were discarded, cells were washed with PBS and incubated with fresh medium along 30 min at room temperature (RT). Then, one volume of CellTiter-Glo® reactive was added to cell media in each well, stirred 2 min in an orbital shaker and incubated 10 min at RT until signal stabilization. The luminescence of each well was measured in a Cytation 5 instrument.

2.13 Induction of apoptosis-necrosis

2.13 a Nanovesicles induction of apoptosis/necrosis on J774A.1 cells, was determined by flow cytometry employing YO-PRO™-1 and PI dyes. Briefly, J774A.1 cells were seeded in 48-wells plates at a density of 7.5 × 10^4 cells per well and grown for 24 h. Then, cells were incubated as state in 2.9. After that, supernatants were discarded, cells were trypsinized and washed twice with PBS. Cell pellets were resuspended in 200 µl PBS containing 0.5 µM YO-PRO™-1 and incubated 15 min at RT. After that, 1 µL of 0.1 mg/ml PI was added to each tube and incubated 5 min on ice. A total 1×10^4 cells were analysed by flow cytometry in a FACS instrument employing a 488 nm laser excitation and collecting the fluorescence in the FL-1 channel for YO-PRO™-1 and FL-3 for PI. A positive control for apoptosis was carried out 18 h before the staining by submitting the cells to UV irradiation along 15 min. A positive control for necrosis was carried out by incubating cells with 500 mM H_2O_2 in PBS for 3 h before the staining.

2.13 b. Cell morphology and YO-PRO™-1, PI and Hoescht staining upon nanovesicles incubation was determined by microscopy. Briefly, once the incubation was finished, the media was discarded, washed once with PBS and 1 ml of cold PBS was added. 1 µL of 100 µM YO-PRO solution was added; after 15 min, 1 µL of 0.1 mg/mL PI solution and 20 µL of 0.1 mg/mL Hoescht solution were added. Immediately, the cells were observed in a Cytation 5 instrument (YO-PRO was observed with the fluorescence cube YFP, PI was observed with the RFP cube, and Hoescht with the DAPI cube). Micrographs were taken at 20X.

2.13 c. Late apoptosis was determined by the TUNEL *(Terminal Deoxynucleotide Transferase dUTP Nick End Labeling*) assay. Briefly, J774A.1 cells seeded and incubated with nanovesicles as state **in 2.9.** Upon incubation, cells were washed, collected by trypsinization, cell density was adjusted at ~1 x 10^6 cells/ml in PBS and fixed with 1% w/v paraformaldehyde. The cells were washed twice with PBS, 70% v/v cold ethanol was added, and the cells were stored in -20°C freezer upon further analysis. The degree of fragmentation and total content of DNA were determined employing the APO-BrdU™ TUNEL Assay Kit, (Molecular Probes, Invitrogen (Oregon, USA)) according to manufacturer guidelines. A total of 10.000 cells were analysed in a FACS instrument employing a 488 nm excitation laser and collecting the fluorescence in the FL-1channel for Alexa Fluor 488 and FL-3 for PI.

2.14 Effect of archaeolipids on signalling proteins

Briefly, J774A.1 cells were seeded in 6-wells plates at a density of 1 ×10^6 cells per well and grown for 24 h. Then, cells were incubated as stated in 2.9 with nanoARC or nanoliposomes. After 24 h of incubation the medium was removed, cells were washed with PBS and plates were kept at -80°C until cell solubilization to prepare cells extracts. Cells were homogenized in homogenization buffer (1% v/v Triton, 0.1 M Hepes, 0.1 M sodium pyrophosphate, 0.1 M sodium fluoride, 0.01 M EDTA, 0.01 M sodium vanadate, 0.002 M PMSF, and 0.035 trypsin inhibitory units/ml aprotinin, pH 7.0) at 4°C. Cell homogenates were centrifuged at 15,000 ×g for 40 min at 4°C to remove insoluble material. Protein concentration of supernatants was determined by the BCA protein assay kit. Equal protein aliquots of solubilized cells were diluted in Laemmli buffer, boiled for 5 min, and stored at −20°C until electrophoresis. Samples were subjected to electrophoresis in SDS-polyacrylamide gels. Electro transference of proteins from gel to PVDF membranes and incubation with antibodies were performed as already described [33]. Immunoreactive proteins were revealed by enhanced chemiluminescence. Band intensities were quantified using Gel-Pro Analyzer 4.0 software (Media Cybernetics, Silver Spring, MD, USA). To reprobe with other antibodies, the membranes were washed with acetonitrile for 10 min and then incubated in stripping buffer (2% w/v SDS, 0.100 M 2-mercaptoethanol, 0.0625 M Tris/HCl, pH 6.7) for 40 min at 50°C while shaking, washed with deionized water, and blocked with BSA.

2.15 Induction of ROS/ RNS

Nanovesicles induction of reactive oxygen species (ROS) or reactive nitrogen species (RNS) by J774A. 1 cells upon 24 h incubation with or without LPS was measured using the CM-H2DCFDA dye and Griess method, respectively [34,35]. Briefly, J774A.1 cells were seeded and incubated as state in 2.10 in the absence and presence of 1 µg/ml LPS. RNS was quantified in culture supernatants after precipitating cells and debris, by adding 1 volume of Griess Reactive Solution “A” and 1 volume of Griess Reactive Solution “B”. After 15 min of incubation protected from light, the absorbance was measured at 520 nm in a Cytation 5 instrument. RNS concentrations were calculated by comparison with absorbance at 520 nm of standard calibration solutions made with sodium nitrite from 2.5 to 30 µM.

ROS was quantified in culture cells after washing each well with PBS, by adding 4.4 µg/ml CM-H2DCFDA dye in PBS. After 30 min of incubation at 37ºC in 5% CO_2 atmosphere, cells were washed with PBS and the fluorescence intensity at λ_{ex} 490/10 nm - λ_{em} 530/10 nm was determined in a Cytation 5 instrument.

2.16 Anti-inflammatory activity of nanoarchaeosomes.

The *in vitro* anti-inflammatory activity of nanovesicles was determined by measuring the release of cytokines upon incubation of J774A.1 with LPS. Briefly, J774A.1 cells were seeded and incubated as state in **2.10** in the presence of 1 µg/ml LPS. After 24 h of incubation, supernatants were collected and stored at -20°C until analysis. Mouse TNF-α and IL-6 levels were measured by enzyme-linked immunosorbent assay BD OptEIA™ (BD Biosciences, NJ, USA) following the manufacturer instructions.

2.17 Induction of foam cells (FC) from J774A.1 cells

The uptake of oxidized LDL mediated by cells expressing SRAI lacks negative feedback and is responsible for the generation of foam cells (FC) [16]. FC induction was carried out as described by Ledda et al. 2016 [36]. Briefly, 1.5 × 10^5 J774A.1 cells per well were seeded in 24 wells plates and grown for 24 h. Then, cells were incubated for 24 h with 100 µg/ml of oxLDL (prepared as described by Ledda 2016 from human LDL (see Supplementary info) at 37°C and 5% CO_2 atmosphere.

FC transformation was assessed by Oil Red O (ORO) staining and by morphological analysis by transmission electron microscopy (TEM). For ORO staining, FC cells were fixed to glass coverslips previously placed in 24-wells plates by covering them with 10% formaldehyde in PBS 15 min at RT. After removing fixing buffer carefully, cells were covered with fresh ORO working solution (prepared from a stock solution (0.5 g ORO in 100 ml isopropanol) by adding 6 ml of stock to 4 ml of bidistilled water and filtered through 3 µm filters) for at least 1 h at RT. Then cells were rinsed several times carefully with bidistilled water and allowed to air dry [37]. Cells were visualized under optical microscope Olympus BX51 equipped with Olympus DP-70 camera (Olympus, Japan). The designation of a macrophage as a FC required positive ORO staining [38].

For TEM, J774A.1 were seeded and grown for 24 h in cell culture dish (100 x 20 mm) at a density of 9 × 10^6 cells per dish. FC transformation was carried out and then the cells were harvested using a sterile scrap, washed with PBS and centrifuged at 5000 rpm for 10 min to obtain a cell pellet. The pellet was suspended in 1 ml of 2.5% glutaraldehyde and stored at 4°C

for 4 h. The fixative was washed with PBS at 15 min intervals at 4°C and a second fixation was performed with 1% osmium tetroxide for 60 min at 4°C. The second fixative was washed with bidistilled water and the dehydration of the material was carried out in ascending alcohols (50º, 70º, 96º, 100º), finishing the process with two changes of acetone for 10 min. Then, it was included in epoxy resin allowing polymerizing at 60 ºC for 72 h. To observe the samples, ultrathin sections 70-90 nm thick were cut with an Ultramicrotome Ultracut E (Reichert – Jung, Germany) and mounted on copper grids. Uranyl acetate and lead citrate were used for the contrast and were observed in Zeiss EM 109T (Zeiss International, Germany) equipped with Gatan ES1000W (Gatan Inc. CA, USA) camera.

2.19 Statistical analysis

Statistical analyses were performed by one-way analysis of variance followed by Dunnet's test or two-way analysis of variance followed by Sildak's test using Prisma 4.0 Software (Graph Pad Software, CA, USA). The p-value of <0.05 was considered statistically significant: *p < 0.05; **p <0.01; ***p < 0.001, ****p < 0.0001; n.s. represents non-significant (p > 0.05).

3. Results

3.1Structural features of ALN loaded nanoarchaeosomes

The polar archaeolipids extracted from *Halorubrum tebenquichense*, were identified by ESI-MS by Higa et al. (2012) [17] and ordered according to decrescent abundance as: archaeol analog methyl ester of hosphatidylglycerophosphate (PGPMe), archaeol analog phosphatidylglycerol (PG), (1-O-[a-D-mannose-(2′-SO3H)-(1′ a 2′)-a-D-glucose]- 2,3-di-O-phytanyl-sn-glycerol) (SDGD5) the cardiolipin bis phosphatidylglycerol (BPG) and the glycocardiolipin SDGD5PA (2′-SO3H)-Manp-a1,2Glcpa-1-1-[sn-2,3-di- O phytanylglycerol]-6-[phospho-sn-2,3-di-O-phytanylglycerol]. Recently the double negatively charged PGPMe, majoritarian polar lipid in *H. tebenquichense* responsible for its highly negative Z potential, was confirmed to be a ligand of SRA-1 and not of SRB (the phosphatidylserine receptor) [15,17,23]. The structural features (size, ζ potential, GP and FA, ALN/lipid ratio) are shown in Table 1. The more ordered bilayers of nanoARC-Chol (ALN), displayed a higher ALN/lipid ratio than nanoARC(ALN) (50 vs 38 μg ALN/mg lipid). Our formulations at (6.3 mg/ml) (7 mM lipid) provided an ALN concentration varying between 322-234 μg ALN/ml (~0.7-1 mM ALN).

Laurdan is sensitive to membrane phase transitions and other alterations to membrane fluidity. When the membrane is in a fluid phase, the reorientation rate is faster than the emission process, and consequently, a red shift at λex=340 nm from about 435 nm to about 480 nm is observed [39]. The generalized polarization (GP) quantifies this red shift from the emission spectra. ''Order'' can be defined as representing conformational order of the phospholipid molecules (mostly based on the acyl chains) and "fluidity" as representing the ability of lipids to diffuse in the plane of the bilayer and/or rotate [40]. The change from disordered toward ordered phases represents an actual loss of water molecules from the bilayers. Since fluorescence anisotropy (FA) reports changes in membrane fluidity while GP is more sensitive to variations in membrane order [41], both changes in order and fluidity of structural modified nanovesicles were here assessed by Laurdan GP and FA. Because of the perpendicular methyl groups in isopranyl chains, nanoARC bilayers are known to be packed loosely, entropic and disordered, compared to the rigid bilayers of nanoliposomes made of HSPC-chol [42,43]. The lateral entanglement of methyl groups and the bulky carbohydrate moieties from sugar headgroups connected by hydrogen bonds, account for a reduced lateral diffusion (a feature associated to fluidity) [44]. The addition of cholesterol to nanoARC bilayer increased its order but did not perturb its fluidity. ALN on the other hand, increased the disorder of nanoARC (ALN), and fluidity of all bilayers (including that of HSPC-chol), suggesting that, besides of trapped in the aqueous space, ALN may also be partitioned in lipid bilayers. Fig 1 A and B shows representative Cryo-EM images of nanoARC and nano-ARC(ALN), which consisted of uni or oligolamellar nanovesicles.

3.1.1. Adsorption of human serum proteins on nanoARC bilayer

It was observed first, as judged by the higher SPR angle shift (Fig. 2, Table 2), that nanoARC adsorbed to the Au derivatised surface in lesser extent than control nanoliposomes made of phospholipids of comparable ξ potential. Attached nanoARC was submitted to a 10ul/min serum proteins flow and acquired a higher mass of proteins corona than control nanoliposomes of matching size and ξ potential; the nanoARC corona was slightly desorbed as a function of time. No adsorption of PLA2 was sensed on nanovesicles surface (probably because of its low concentration of 5 μg/ml), but while injected, a loss of mass in nanoliposomes was detected, probably because of hydrolytic activity of PLA2. Instead, no changes were

registered on nanoARC sensorgram, suggesting than nanoARC bilayer were less sensitive to PLA2 than nanoliposomes.

3.2 ALN release upon nanovesicles dilution

Upon submitted to a 1/200 dilution in albumin containing buffer, a significant increase of size and PDI of HSPC-chol(ALN) was observed after 3 h, together with a 40 % loss of its ALN content. On the contrary, size and PDI of nanoARC(ALN) and nanoARC-chol(ALN) remained unchanged, releasing ~1 and 8-9 % of their ALN content, respectively (Fig. 3 A and B).

3.3 Uptake of nanovesicles by J774A.1 cells

The uptake of RhoPE labeled nanovesicles by J774A.1 was measured by flow cytometry. A rough estimation of the uptake rate, by determining the extent of uptake [RhoPE fluorescence] as a function of time, showed that nanoARC and nanoARC-chol were massively internalized after 5 h, both at nearly 20 folds higher extent than HSPC-chol by J774A.1 (Fig. 4). Because of the different ALN/lipid ratio, nanoARC(ALN) delivered ALN at a 0.7 folds lower rate than nanoARC-chol(ALN); in other words, upon the same incubation time with nanoarchaeosomes, the cells internalized the same amount of archaeolipids (equal uptake rate), but less ALN (lower ALN/lipid ratio) from nanoARC(ALN). The preincubation of nanovesicles with human plasma did not modify the rough uptake rate.

3.4 Nanovesicles cytotoxicity

Free ALN is reported to be cytotoxic on J774A.1 at 10^{-4} M [21]. Here we found that between 10 and 500 μg lipids/ml, HSPC-chol(ALN) and free ALN between **10-500** μg ALN/ml**,** were not cytotoxic on J774A.1. The cytotoxicity of nanoarchaeosomes instead, was dependent of their lipid composition and of the presence of ALN: the cell viability was reduced by 50 % by 100 μg lipids/ml nanoARC(ALN), ~ 500 μg lipids/ml nanoARC-chol(ALN), ~ 500 μg lipids /ml nanoARC and >> 500 μg/ml nanoARC-chol (Fig 5A). Remarkably, while nanoARC(ALN) at 100 μg lipids/ml containing (3.3-5 μg ALN/ml ~ 10 μM =10^{-5} M) decreased by 50 % the cell viability, free ALN at 100 μg ALN/ml (~30 folds higher concentration) was not cytotoxic. Cytotoxicity followed the same trend after 48 h (Fig. 5B).

3.5 Induction of acid vesicles

Acidotropic lysotracker dyes such as LR, non-specifically stain acidic compartments such as the increased lysosomal mass observed during autophagy, or autophagosomes, even if autophagic flux is blocked. The LR fluorescence may indirectly quantify the degree of autophagy, since its increase follows that of the autophagy marker LC3II [45]. No changes in LR fluorescence were registered after incubating 100 μg lipids/ml HSPC-chol(ALN) along 24 h. However, after incubating 100 μg lipids/ml nanoarchaeosomes, a 6-10 folds increase in fluorescence was registered (Fig 6A). The fluorescence was kept 2.5 folds increased, 24 h after nanoarchaeosomes were removed and replaced by fresh media (supplementary figure 1A**).** Nanoarchaeosomes display a highly negative ζ potential and are not expected to induce lysosomal damages type sponge effect induced by cationic nanoparticles, where lysosomal integrity is lost [46], and lysosomal proteases are released into the cytosol [47] evidenced as a fast loss of LR fluorescence [48]. The increased cytoplasmic fluorescence induced by nanoarchaeosomes [representative images in Fig. 6D show big sized cytoplasmic acid vesicles after nanoARC and nanoARC-chol uptake and Fig. 1D, a representative electronic micrograph section of a J774A.1 cell upon 24 h of incubation with nanoARC; black arrows pointing a profusion of cytoplasmic vesicles] may correspond to autophagolysosomes, or to non-lethal events such as lysosomal stress with swelling and partial increase in membrane permeability that may trigger lysosome autophagy and further lysosomal biogenesis via TFEB [49]. A slight increase in side scattering (SSC), without changes in forward scattering (FSC) was also detected for nanoarchaeosomes, a sign associated to the induction of acidic vesicles [50] (Supplementary Fig. 1B and C). Overall, the sustained increased fluorescence suggests thus, that nanoarchaeosomes may induce autophagy [45] independently of the presence of ALN.

3.6 Mitochondrial membrane potential (MMP).

The lipophilic and cationic JC-1 dye is able to enter into the mitochondria as a green monomer, where it accumulates and (in a concentration-dependent manner) forms reversible complexes called J- aggregates, of excitation and emission in the red spectrum (maximum at ~590 nm). In healthy cells with a normal MMP, the JC-1 dye enters and accumulates in the energized and negatively charged mitochondria, spontaneously forming red fluorescent J-aggregates. The JC-1 red/green fluorescence ratio thus, is directly related to the mitochondria polarization state: the higher the ΔΨM, the higher the ratio, since more J aggregates are formed at the expenses of green monomer. Accordingly, mitochondrial depolarization is indicated by a reduction in the JC-1 red/green fluorescence ratio [51].

Here we found that the JC-1 red/green ratio was not modified upon incubation 100 μg/ml HSPC-chol(ALN) along 24 h (**fig 6B**). The ratio was reduced by ~40% by nanoARC-chol and nanoARC-chol(ALN), while nanoARC and nanoARC(ALN) caused a lower decrease. Again, as occurred on acid vesicles, ALN had no effect on the MMP reduction caused by nanoarchaeosomes. The JC-1 red/green ratio remained low 24 h after nanoarchaeosomes were washed and replaced by fresh media, meaning the changes were irreversible (supplementary Fig 1 D). The reduction in MMP, usually regarded as the "point-of-no-return" in cell death [52,53], can be caused by cathepsins released from damaged lysosomes, which activate proapoptotic proteins, and permeabilize mitochondria membrane (between other events such as activation of caspase 3/7 and cleavage of PARP-1) [54,55] . MMP reduction associated to lysosomal damage, has been evidenced nearly 5-10 h after endocytic uptake of toxic cationic nanoparticles [56]. The MMP reduction observed here, may be ascribed to non-lethal lysosomal perturbations upon nanoarchaeosomes internalization, since it took place in absence of lysosomal destruction and with unchanged forward scattering, which is reported to be reduced when MMP is lost [57].

3.7 Mitophagy

Upon 24 h of incubation with 100 μg lipids/ml nanoarchaeosomes, no co-localization of LG and MR was observed in J774A.1 cells (Fig. 6D), as judged by the low Pearson's correlation coefficient (nanoARC(ALN) 0.66 ± 0.10; nanoARC-chol(ALN) 0.36 ± 0.09 and HSPC-chol(ALN) 0.54 ± 0.05; n = 5).

3.8 Intracellular ATP content

Upon 24 h of incubation with 100 μg lipids/ml nanoarchaeosomes, no decrease in intracellular ATP content of J774A.1 cells was registered (Fig. 6C).

3.9 Induction of apoptosis-necrosis

After 24 h of incubation with 100 μg lipids/ml nanoarchaeosomes, the highest cytotoxicity on J774A.1 cells was caused by nanoARC(ALN), that induced the highest degree of early apoptosis (Fig. 7A).

Clear field and fluorescence microscopy images of cells incubated with nanoARC were taken to assess cell morphology and stain density with Hoescht. Upon incubated 24 h with 100 μg/mL nanoARC, vacuoles appaired and the cells size was reduced, some few were stained with YO-PRO but not with IP (Fig. 7B). Upon incubated 24 h with 500 μg/mL nanoARC, the cells became poorly adherent, with poorly defined borders and vacuoles increased, positive for YO-PRO and IP and more brilliant staining with Hoescht in some nuclei sectors, suggesting more condensed chromatin (Supplementary Fig. 2)

The TUNEL assay was performed to determine the degree of DNA fragmentation, a marker of late apoptosis. Cells irradiated with UV light increased the amount of fragmented DNA and of fluorescence intensity (FI), in comparison to the FI of control cells. No DNA fragmentation was detected in cells incubated with nanoliposomes between 50 and 500 μg/mL or nanoARC up to 100 μg/mL, but increased FI of cell was observed for 500 μg/mL nanoARC (Supplementary Fig 3)

3.10 Effect of archaeolipids on signalling proteins

The amounts of signalling proteins AKT/pAKT and ERK/pERK upon 24 h of incubation with nanoARC or nanoliposomes made of SPC (191 ± 7 nm; PDI 0.2 ± 0.005; ζ potential -3.2 ± 0.5) was determined by Western Blot. The Akt1 protein is widely distributed in body tissues and is involved in growing and cell survival. Several growing factors and cytokines activate signalling cascades ending up with the activation (phosphorylation) of AKT as pAKT [58]. Here it was found that the levels of AKT and pAKT remained unchanged (Fig. 8). The extracellular signals related kinases (ERK) belong to the signalling routes of mitogen activated protein kinases (MAPK). Such signalling route responds mainly to growing factors and mitogens that control growing, cell proliferation, survival, and death. The cytoplasmic enzyme ERK is activated by phosphorylation as pERK. Once activated it is translocated to the nuclei, where activates transcription factors inducing the expression of gene that promote cell survival, division, and motility [59]. Here we found that from 100 μg/mL nanoARC increased pERK but not ERK (Fig. 8)

3.11 Induction of ROS/ RNS

Upon 24 h of incubation with 100 μg lipids/ml nanoarchaeosomes, no induction of ROS was observed. In presence of LPS however, the induced ROS was significantly reduced by nanoarchaeosomes, but not by HSPC-chol(ALN) (Fig. 9A). on the other hand, nanoarchaeosomes increased the levels of RNS, and the RNS levels raised by LPS were significantly decreased only by nanoARC-chol and nanoARC-chol(ALN) (Fig. 9B). The presence

of ALN seemed not to play a role in the levels of reactive oxygen and nitrogen species. The induction of ROS by nanoarchaeosomes as a cause of mitochondrial damage should thus be discarded.

3.12 Anti-inflammatory activity

Upon 24 h of incubation with 100 μg lipids/ml nanoarchaeosomes, the release of IL-6 was significantly reduced by nanoarchaeosomes (Fig. 10A). No effect on the release of TNF-α was registered (Fig. 10B)

3.13 Induction of FC from J774A.1 and nanovesicles cytotoxicity on FC

Induction of FC was performed by incubating J774A.1 cells with oxLDL followed by assessment by Oil Red O staining (supplementary Fig. 4 A and B profusion of cytoplasmic lipid droplets). FC were more susceptible to nanoarchaeosomes than J774A.1 cells: ~25 μg/ml nanoARC(ALN) and ~ 50 μg/ml nanoARC-chol(ALN), reduced by 50 % the cell viability**.** HSPC-chol(ALN) and free ALN, reduced by 25 % the cell viability, in a concentration independent fashion supplementary Fig. 5A and B. The FC are defective in autophagy [60] and in cholesterol efflux [61]. The higher cytotoxicity of nanoarchaeosomes would be owed to the inherent difficulty of FC to recycle or eliminate archaeolipids and/or cholesterol; in healthy J774A.1 cells instead, these mechanisms are functional, and these molecules cause less cytotoxicity. In advanced atherosclerosis, the FC have a key role in perpetuating the inflammatory state [62–64]. Killing monocytes/macrophages from early stages plaque have been evaluated as a therapeutic strategy [65] but in advanced plaque the induction of FC apoptosis should be avoided, since it would lead to secondary necrosis in an environment of diminished efferocytosis, contributing to plaque destabilization [66].

4. Discussion and conclusions:

This is the first report employing nanoarchaeosomes as killer agents' carriers, specifically ALN-aided targeted nanoparticulate macrophage killers. In such frame, two nanoarchaeosomal ALN formulations: nanoARC(ALN) and nanoARC-chol(ALN), were prepared and characterized. Intended to shift ALN biodistribution towards extra-bone macrophages, nanoarchaeosomal ALN was expected to be highly endocytosed by macrophages, and more efficient apoptotic inducer than free ALN, because of providing a massive intracellular delivery of ALN. The ALN/lipid ratio of nanoARC(ALN) and nanoARC-chol(ALN) was low, between 12 and 9 folds lower respectively than the 1,22 ALN/lipid ratio of distearoyl phosphatidylcholine, distearoyl phosphatidylglycerol and cholesterol DSPC:DSPG:chol(ALN) developed as antirestenosis agent [67]. But when it comes to endocytosed formulations, the amount of internalized ALN is a function not only of the ALN/lipid ratio but on the formulation uptake rate. Here we observed that nanoarchaeosomes were internalized at a 20 folds higher rate than HSPC-chol(ALN) nanoliposomes, satisfying the need for massive ALN delivery that would lead to higher cytotoxicity. But it was also observed as well that, despite of delivering less ALN than nanoARC-chol(ALN), nanoARC(ALN) caused the highest cytotoxicity to J774A.1 cells. Therefore, opposite to what it was first speculated (higher intracellular delivery of ALN, higher cytotoxicity), the cytotoxicity on J774A.1 cells would not be owed to a massive ALN internalization, but to the intake of a combination of pure archaeolipids (from nanoARC) and ALN. Another interesting finding was that archaeolipids cytotoxicity seemed to be reduced by the presence of cholesterol. We had previously reported that archaeolipids and phospholipids or NaChol may form non-covalent complexes [68]. The elimination of putative archaeolipids-cholesterol complexes via cholesterol efflux mechanisms, may decrease the intracellular accumulation of archaeoliopids, explaining the lower cytotoxicity of nanoARC-chol compared to that of nanoARC. The involved mechanisms will be subject of further studies.

Nanoliposomal bisphosphonates must be administered by endovenous route and in humans are submitted to important dilutions, that may cause cargo leakage. Available data on stability of ALN nanoliposomes made of DSPC:DSPG:chol (ALN) for instance, are reported for a dose of 30 mg ALN/ kg rabbit, which corresponds to a dilution factor of 1/8 [67]. In a previous report, however, doses 5-10 folds lower were administered, corresponding to higher dilution factors, in the order of 1/80 (assuming equal initial lipid concentrations) [69]. Moreover, assuming always 20 mM lipid and 24.5 mM ALN concentrations reported in [67] and [69], in the clinical BLADE-PCI trial [12] for example and 80 μg ALN per human body was administered, which corresponds to 10 μL of a formulation suffering a ~ 1/ 350.000 folds dilution. Such a high dilution factor, despite of the encouraging results obtained in animal models may perturb the stability of nanoliposomal ALN. Here we observed that, despite of displaying low and comparable ALN/lipid ratio, nanoarchaeosomes and nanoliposomes responded different when

submitted to dialysis against a 1/200 dilution: both nanoARC(ALN) and nanoARC-chol(ALN) retained most of ALN whereas rigid HSPC-chol (ALN), lost nearly 50% of its ALN content after 3 h. Nanoarchaeosomes bilayers are known to be less permeable to protons and hydroxyls than those of nanoliposomes [43] keeping hydrosoluble drugs within the inner space while submitted to shear stress [15]. Such structural features of nanoarchaeosomes may have contributed to the high retention of ALN upon dilution.

A stable entrapment during dilution and the potential for targeted delivery, are key factors that will shape pharmacokinetics, biodistribution and pharmacodynamics of ALN in nanoarchaeosomes. As screened by SPR, different to nanoliposomes, the nanoARC bilayer remained refractory to hydrolytic activity of PLA2. Presumably, the *sn*2,3 stereoisomery of archaeolipids [different from *sn*1,2 of phospholipids from Eukarya and Bacteria origin [14], together with the ether instead of ester bonds to the glycerol backbone, explained why archaeolipids would not constitute suitable substrates for hydrolytic activity of PLA2. *In vivo*, both the release of ALN upon dilution and the attack of hydrolytic enzymes would favour the early destruction of carriers and ALN loss. The released ALN would rapidly bind to the bone matrix, not being available to tissue macrophages or circulating monocytes. Taken together, these results suggest that nanoarchaeosomes, by being less affected by dilution, shear stresses, or hydrolytic proteins, are worth to be explored as targeted nanocarriers for parenteral administration alternative to ordinary nanoliposomes.

Finally, several effects caused by nanoarchaeosomes were found to be independent from chol or ALN content. For instance, nanoarchaeosomes (and not HSPC-chol/(ALN) or free ALN) at 100 μg lipids/ml were not only not pro-inflammatory, but also strongly reduced the induction of ROS and of IL-6, and of RNS in lesser extent, upon LPS stimulus on J774A.1 cells. The antiinflammatory effect was equally induced by the cytotoxic nanoARC(ALN) and by the innocuous nanoARC-Chol. By combining poor cytotoxicity and high macrophage internalization, nanoARC-Chol deserve thus to be explored as anti-inflammatory agent, alternative to classical glucocorticoids or non-steroid anti-inflammatory agents. Indeed, archaeolipids and ordinary phospholipids affected differently vital organelles, such as the interconnected signalling platforms mitochondria-lysosomes [70]: only nanoarchaeosomes reduced by 20-40 % MMP in the absence of ROS and of mitophagy, without neither perturbing lysosomal integrity, nor inducing ATP consumption. All nanoarchaeosomes (devoid or ALN loaded) strongly induced acid vesicles [a signal of impaired autophagic flux or of increased lysosomal biogenesis [71] (Fig. 1 D) both events related to autophagy]; only archaeolipids induced pERK. The significance of the activation of a map kinase with multiple downstream substrates such as ERK [72] and within the above-mentioned context, will be addressed in further studies. S*imilitudes between nanoarchaeosomes and nanoliposomes ends up in forming sealed vesicles in aqueous media, since a*rchaeolipids metabolization generates downstream signals divergent from those induced by ordinary phospholipids.

The present study showing massive endocytosis of nanoarchaeosomes was performed on the mouse J774A.1 cell line expressing SRA-1 [73]. In humans however, the expression level of SRA1 by normal THP1 monocytes/macrophages is low [74,75], meaning the SRA1 dependent internalization of nanoarchaeosomes by circulating monocytes is expected to be low. Nonetheless, human monocytes/macrophages are known to increase the expression of SRA1 upon LPS stimuli or in front to diverse types of stress, such as anomalous shear forces within the vessel intima [76]. As a whole, these preliminary results suggest that, as far as efferocytosis is not diminished, apoptotic death of chronically activated inflammatory macrophages such as those found in restenosis, tumours, alveoli [77] and arthritis rheumatoid, could be induced with macrophage targeted cytotoxic nanoARC(ALN), while nanoARC-Chol may be explored as anti-inflammatory macrophage targeted agent.

Acknowledgements

This work was supported by Secretaria de Investigaciones, Universidad Nacional de Quilmes under Grant Nanomedicinas-2. HEJ has fellowships from National Council for Scientific and Technological Research (CONICET). ELR, MJM and MJA are members of the Research Career Program from CONICET.

Credit roles

Horacio Emanuel Jerez: Methodology, formal analysis and writing-original draft

Maria Julia Altube:	Methodology
Yamila B Gándola:	Methodology
Lorena González:	Methodology
Marina Cecilia Gonzalez:	Methodology
Maria Jose Morilla:	Formal analysis, writing-original draft and funding acquisition
Eder Lilia Romero:	Conceptualization, supervision, writing-review & editing and funding acquisition

References

[1] M.J. O'Neil, The merck indexan encyclopedia of chemicals, drugs, and biologicals, 2006.

[2] B.J. Gertz, S.D. Holland, W.F. Kline, B.K. Matuszewski, A.G. Porras, Clinical pharmacology of alendronate sodium, Osteoporos. Int. 3 (1993) 13–16.

[3] M.T. Drake, B.L. Clarke, S. Khosla, Bisphosphonates: mechanism of action and role in clinical practice, in: Mayo Clin. Proc., Elsevier, 2008: pp. 1032–1045.

[4] H. Mönkkönen, S. Auriola, P. Lehenkari, M. Kellinsalmi, I.E. Hassinen, J. Vepsäläinen, J. Mönkkönen, A new endogenous ATP analog (ApppI) inhibits the mitochondrial adenine nucleotide translocase (ANT) and is responsible for the apoptosis induced by nitrogen-containing bisphosphonates, Br. J. Pharmacol. 147 (2006) 437–445.

[5] M. Sato, W. Grasser, N. Endo, R. Akins, H. Simmons, D.D. Thompson, E. Golub, G.A. Rodan, Bisphosphonate action. Alendronate localization in rat bone and effects on osteoclast ultrastructure., J. Clin. Invest. 88 (1991) 2095–2105.

[6] H. Fleisch, Bisphosphonates in bone disease: from the laboratory to the patient, Elsevier, 2000.

[7] J.H. Lin, I.W. Chen, D.E. Duggan, Effects of dose, sex, and age on the disposition of alendronate, a potent antiosteolytic bisphosphonate, in rats., Drug Metab. Dispos. 20 (1992) 473–478.

[8] N. Van Rooijen, A. Sanders, Liposome mediated depletion of macrophages: mechanism of action, preparation of liposomes and applications, J. Immunol. Methods. 174 (1994) 83–93.

[9] N.O. Hodgins, J.T.W. Wang, A.C. Parente-Pereira, M. Liu, J. Maher, K.T. Al-Jamal, In vitro potency, in vitro and in vivo efficacy of liposomal alendronate in combination with γδ T cell immunotherapy in mice, J. Control. Release. 241 (2016) 229–241.

[10] H.D. Danenberg, I. Fishbein, J. Gao, J. Mönkkönen, R. Reich, I. Gati, E. Moerman, G. Golomb, Macrophage depletion by clodronate-containing liposomes reduces neointimal formation after balloon injury in rats and rabbits, Circulation. 106 (2002) 599–605.

[11] B.J. Burwitz, J.S. Reed, K.B. Hammond, M.A. Ohme, S.L. Planer, A.W. Legasse, A.J. Ericsen, Y. Richter, G. Golomb, J.B. Sacha, Technical advance: liposomal alendronate depletes monocytes and macrophages in the nonhuman primate model of human disease, J. Leukoc. Biol. 96 (2014) 491–501.

[12] P. Généreux, BLADE-PCI: Novel liposomal alendronate fails in diabetes, Cardiol. Today. (2019). https://www.healio.com/news/cardiac-vascular-intervention/20191004/bladepci-novel-liposomal-alendronate-fails-in-diabetes (accessed August 18, 2020).

[13] What Are The Differences Between (Advantages Of) Synthetic And Natural Phospholipids? | Avanti Polar Lipids, (n.d.). https://avantilipids.com/tech-support/faqs/synthetic-vs-natural-phospholipids (accessed August 18, 2020).

[14] A. Corcelli, S. Lobasso, 25 characterization of lipids of halophilic archaea, in: Methods Microbiol., Elsevier, 2006: pp. 585–613.

[15] M.J. Altube, S.M. Selzer, M.A. de Farias, R.V. Portugal, M.J. Morilla, E.L. Romero, Surviving nebulization-induced stress: dexamethasone in pH-sensitive archaeosomes, Nanomedicine. 11 (2016) 2103–2117.

[16] J. Han, A.C. Nicholson, Lipoproteins modulate expression of the macrophage scavenger receptor., Am. J. Pathol. 152 (1998) 1647.

[17] L.H. Higa, P. Schilrreff, A.P. Perez, M.A. Iriarte, D.I. Roncaglia, M.J. Morilla, E.L. Romero, Ultradeformable archaeosomes as new topical adjuvants, Nanomedicine Nanotechnology, Biol. Med. 8 (2012) 1319–1328.

[18] L.H. Higa, H.E. Jerez, M.A. De Farias, R.V. Portugal, E.L. Romero, M.J. Morilla, Ultra-small solid archaeolipid nanoparticles for active targeting to macrophages of the inflamed mucosa, Nanomedicine. 12 (2017). https://doi.org/10.2217/nnm-2016-0437.

[19] M.J. Altube, A. Cutro, L. Bakas, M.J. Morilla, E.A. Disalvo, E.L. Romero, Nebulizing novel multifunctional nanovesicles: the impact of macrophage-targeted-pH-sensitive archaeosomes on a pulmonary surfactant, J. Mater. Chem. B. 5 (2017) 8083–8095.

[20] F.L. Parra, A.T. Caimi, M.J. Altube, D.E. Cargnelutti, M.E. Vermeulen, M.A. de Farias, R.V. Portugal, M.J. Morilla, E.L. Romero, Make it simple:(Sr-A1+ TLR7) macrophage targeted NANOarchaeosomes, Front. Bioeng. Biotechnol. 6 (2018) 163.

[21] M.-F. Moreau, C. Guillet, P. Massin, S. Chevalier, H. Gascan, M.-F. Baslé, D. Chappard, Comparative effects of five bisphosphonates on apoptosis of macrophage cells in vitro, Biochem. Pharmacol. 73 (2007) 718–723.

[22] A.T. Caimi, F. Parra, M.A. de Farias, R.V. Portugal, A.P. Perez, E.L. Romero, M.J.

Morilla, Topical vaccination with super-stable ready to use nanovesicles, Colloids Surfaces B Biointerfaces. 152 (2017) 114–123.
[23] R.O. Gonzalez, L.H. Higa, R.A. Cutrullis, M. Bilen, I. Morelli, D.I. Roncaglia, R.S. Corral, M.J. Morilla, P.B. Petray, E.L. Romero, Archaeosomes made of Halorubrum tebenquichensetotal polar lipids: a new source of adjuvancy, BMC Biotechnol. 9 (2009) 71.
[24] M. Kates, S.C. Kushwaha, Isoprenoids and polar lipids of extreme halophiles, Archaea, a Lab. Manual. Halophiles. Cold Spring Harb. Lab. Press. Cold Spring Harb. (1995) 35–54.
[25] C.J.F. Bottcher, A rapid and sensitive sub-micro phosphorus determination, Anal. Chim. Acta. 24 (1961) 203.
[26] D.W. Fry, J.C. White, I.D. Goldman, Rapid separation of low molecular weight solutes from liposomes without dilution, Anal. Biochem. 90 (1978) 809–815.
[27] E.G. Bligh, W.J. Dyer, A rapid method of total lipid extraction and purification, Can. J. Biochem. Physiol. 37 (1959) 911–917.
[28] C.A. Schneider, W.S. Rasband, K.W. Eliceiri, NIH Image to ImageJ: 25 years of image analysis, Nat. Methods. 9 (2012) 671–675.
[29] J. Schindelin, I. Arganda-Carreras, E. Frise, V. Kaynig, M. Longair, T. Pietzsch, S. Preibisch, C. Rueden, S. Saalfeld, B. Schmid, Fiji: an open-source platform for biological-image analysis, Nat. Methods. 9 (2012) 676–682.
[30] R.Y. Hampton, D.T. Golenbock, M. Penman, M. Krieger, C.R.H. Raetz, Recognition and plasma clearance of endotoxin by scavenger receptors, Nature. 352 (1991) 342–344.
[31] R. Haworth, N. Platt, S. Keshav, D. Hughes, E. Darley, H. Suzuki, Y. Kurihara, T. Kodama, S. Gordon, The macrophage scavenger receptor type A is expressed by activated macrophages and protects the host against lethal endotoxic shock, J. Exp. Med. 186 (1997) 1431–1439.
[32] C. Zhao, Z. Chen, X. Xu, X. An, S. Duan, Z. Huang, C. Zhang, L. Wu, B. Zhang, A. Zhang, Pink1/Parkin-mediated mitophagy play a protective role in cisplatin induced renal tubular epithelial cells injury, Exp. Cell Res. 350 (2017) 390–397.
[33] Y.B. Gándola, S.E. Pérez, P.E. Irene, A.I. Sotelo, J.G. Miquet, G.R. Corradi, A.M. Carlucci, L. Gonzalez, Mitogenic effects of phosphatidylcholine nanoparticles on MCF-7 breast cancer cells, Biomed Res. Int. 2014 (2014).
[34] P. Schilrreff, Y.R. Simioni, H.E. Jerez, A.T. Caimi, M.A. de Farias, R. Villares Portugal, E.L. Romero, M.J. Morilla, Superoxide dismutase in nanoarchaeosomes for targeted delivery to inflammatory macrophages, Colloids Surfaces B Biointerfaces. 179 (2019). https://doi.org/10.1016/j.colsurfb.2019.03.061.
[35] J.Y. Jang, D.Y. Lee, S.J. Park, Y. Byun, Immune reactions of lymphocytes and macrophages against PEG-grafted pancreatic islets, Biomaterials. 25 (2004) 3663–3669.
[36] A. Ledda, M. González, J. Gulfo, I.D. Ludovico, N. Ramella, J. Toledo, H. Garda, M. Grasa, M. Esteve, Decreased OxLDL uptake and cholesterol efflux in THP1 cells elicited by cortisol and by cortisone through 11β-hydroxysteroid dehydrogenase type 1, Atherosclerosis. 250 (2016) 84–94.
[37] D.E. McVean, R.L. Patrick, C.E. Witchett, An aqueous oil red O fixative stain for histological preparations, Am. J. Clin. Pathol. 43 (1965) 291–293.
[38] L. Chávez-Sánchez, M.G. Garza-Reyes, J.E. Espinosa-Luna, K. Chávez-Rueda, M.V. Legorreta-Haquet, F. Blanco-Favela, The role of TLR2, TLR4 and CD36 in macrophage activation and foam cell formation in response to oxLDL in humans, Hum. Immunol. 75 (2014) 322–329.
[39] M.J. Sheffield, B.L. Baker, D. Li, N.L. Owen, M.L. Baker, J.D. Bell, Enhancement of Agkistrodon piscivorus piscivorus venom phospholipase A2 activity toward phosphatidylcholine vesicles by lysolecithin and palmitic acid: studies with fluorescent probes of membrane structure, Biochemistry. 34 (1995) 7796–7806.
[40] H.A. Wilson-Ashworth, Q. Bahm, J. Erickson, A. Shinkle, M.P. Vu, D. Woodbury, J.D. Bell, Differential detection of phospholipid fluidity, order, and spacing by fluorescence spectroscopy of bis-pyrene, prodan, nystatin, and merocyanine 540, Biophys. J. 91 (2006) 4091–4101.
[41] F.M. Harris, K.B. Best, J.D. Bell, Use of laurdan fluorescence intensity and polarization to distinguish between changes in membrane fluidity and phospholipid order, Biochim. Biophys. Acta (BBA)-Biomembranes. 1565 (2002) 123–128.
[42] K. Yamauchi, K. Doi, Y. Yoshida, M. Kinoshita, Archaebacterial lipids: highly proton-impermeable membranes from 1, 2-diphytanyl-sn-glycero-3-phosphocoline, Biochim.

Biophys. Acta (BBA)-Biomembranes. 1146 (1993) 178–182.
[43] T. Kitano, T. Onoue, K. Yamauchi, Archaeal lipids forming a low energy-surface on air-water interface, Chem. Phys. Lipids. 126 (2003) 225–232.
[44] T. Róg, I. Vattulainen, A. Bunker, M. Karttunen, Glycolipid membranes through atomistic simulations: effect of glucose and galactose head groups on lipid bilayer properties, J. Phys. Chem. B. 111 (2007) 10146–10154.
[45] S. Chikte, N. Panchal, G. Warnes, Use of LysoTracker dyes: a flow cytometric study of autophagy, Cytom. Part A. 85 (2014) 169–178.
[46] M.E. Guicciardi, M. Leist, G.J. Gores, Lysosomes in cell death, Oncogene. 23 (2004) 2881–2890.
[47] C. Oberle, J. Huai, T. Reinheckel, M. Tacke, M. Rassner, P.G. Ekert, J. Buellesbach, C. Borner, Lysosomal membrane permeabilization and cathepsin release is a Bax/Bak-dependent, amplifying event of apoptosis in fibroblasts and monocytes, Cell Death Differ. 17 (2010) 1167–1178.
[48] R. Wang, P.S. Billone, W.M. Mullett, Nanomedicine in action: An overview of cancer nanomedicine on the market and in clinical trials., J. Nanomater. (2013).
[49] F. Wang, R. Gómez-Sintes, P. Boya, Lysosomal membrane permeabilization and cell death, Traffic. 19 (2018) 918–931.
[50] M.G. Bexiga, J.A. Varela, F. Wang, F. Fenaroli, A. Salvati, I. Lynch, J.C. Simpson, K.A. Dawson, Cationic nanoparticles induce caspase 3-, 7-and 9-mediated cytotoxicity in a human astrocytoma cell line, Nanotoxicology. 5 (2011) 557–567.
[51] S.T. Smiley, M. Reers, C. Mottola-Hartshorn, M. Lin, A. Chen, T.W. Smith, G.D. Steele, L.B. Chen, Intracellular heterogeneity in mitochondrial membrane potentials revealed by a J-aggregate-forming lipophilic cation JC-1., Proc. Natl. Acad. Sci. 88 (1991) 3671–3675.
[52] G. Kroemer, B. Dallaporta, M. Resche-Rigon, The mitochondrial death/life regulator in apoptosis and necrosis, Annu. Rev. Physiol. 60 (1998) 619–642.
[53] D.R. Green, J.C. Reed, Mitochondria and apoptosis, Science (80-.). (1998) 1309–1312.
[54] P. Boya, G. Kroemer, Lysosomal membrane permeabilization in cell death, Oncogene. 27 (2008) 6434–6451.
[55] V. Stoka, B. Turk, S.L. Schendel, T.-H. Kim, T. Cirman, S.J. Snipas, L.M. Ellerby, D. Bredesen, H. Freeze, M. Abrahamson, Lysosomal protease pathways to apoptosis cleavage of Bid, not pro-caspases, is the most likely route, J. Biol. Chem. 276 (2001) 3149–3157.
[56] F. Wang, L. Yu, M.P. Monopoli, P. Sandin, E. Mahon, A. Salvati, K.A. Dawson, The biomolecular corona is retained during nanoparticle uptake and protects the cells from the damage induced by cationic nanoparticles until degraded in the lysosomes, Nanomedicine Nanotechnology, Biol. Med. 9 (2013) 1159–1168.
[57] F. Wang, M.G. Bexiga, S. Anguissola, P. Boya, J.C. Simpson, A. Salvati, K.A. Dawson, Time resolved study of cell death mechanisms induced by amine-modified polystyrene nanoparticles, Nanoscale. 5 (2013) 10868–10876. https://doi.org/10.1039/C3NR03249C.
[58] I. Hers, E.E. Vincent, J.M. Tavaré, Akt signalling in health and disease, Cell. Signal. 23 (2011) 1515–1527.
[59] R. Roskoski Jr, ERK1/2 MAP kinases: structure, function, and regulation, Pharmacol. Res. 66 (2012) 105–143.
[60] I. Sergin, B. Razani, Self-eating in the plaque: what macrophage autophagy reveals about atherosclerosis, Trends Endocrinol. Metab. 25 (2014) 225–234.
[61] V. Guerrini, M.L. Gennaro, Foam cells: one size doesn't fit all, Trends Immunol. 40 (2019) 1163–1179.
[62] B. Razani, C. Feng, T. Coleman, R. Emanuel, H. Wen, S. Hwang, J.P. Ting, H.W. Virgin, M.B. Kastan, C.F. Semenkovich, Autophagy links inflammasomes to atherosclerotic progression, Cell Metab. 15 (2012) 534–544.
[63] X. Liao, J.C. Sluimer, Y. Wang, M. Subramanian, K. Brown, J.S. Pattison, J. Robbins, J. Martinez, I. Tabas, Macrophage autophagy plays a protective role in advanced atherosclerosis, Cell Metab. 15 (2012) 545–553.
[64] M. Ouimet, V. Franklin, E. Mak, X. Liao, I. Tabas, Y.L. Marcel, Autophagy regulates cholesterol efflux from macrophage foam cells via lysosomal acid lipase, Cell Metab. 13 (2011) 655–667.
[65] I. Tabas, Macrophage apoptosis in atherosclerosis: consequences on plaque progression and the role of endoplasmic reticulum stress, Antioxid. Redox Signal. 11

(2009) 2333–2339.
[66] D.M. Schrijvers, G.R.Y. De Meyer, M.M. Kockx, A.G. Herman, W. Martinet, Phagocytosis of apoptotic cells by macrophages is impaired in atherosclerosis, Arterioscler. Thromb. Vasc. Biol. 25 (2005) 1256–1261.
[67] H. Epstein, D. Gutman, E. Cohen-Sela, E. Haber, O. Elmalak, N. Koroukhov, H.D. Danenberg, G. Golomb, Preparation of alendronate liposomes for enhanced stability and bioactivity: in vitro and in vivo characterization, AAPS J. 10 (2008) 505–515.
[68] D.C. Carrer, L.H. Higa, M.V.D. Tesoriero, M.J. Morilla, D.I. Roncaglia, E.L. Romero, Structural features of ultradeformable archaeosomes for topical delivery of ovalbumin, Colloids Surfaces B Biointerfaces. 121 (2014) 281–289.
[69] H.D. Danenberg, G. Golomb, A. Groothuis, J. Gao, H. Epstein, R. V Swaminathan, P. Seifert, E.R. Edelman, Liposomal alendronate inhibits systemic innate immunity and reduces in-stent neointimal hyperplasia in rabbits, Circulation. 108 (2003) 2798–2804.
[70] C.M. Deus, K.F. Yambire, P.J. Oliveira, N. Raimundo, Mitochondria–lysosome crosstalk: from physiology to neurodegeneration, Trends Mol. Med. 26 (2020) 71–88.
[71] C. Settembre, C. Di Malta, V.A. Polito, M.G. Arencibia, F. Vetrini, S. Erdin, S.U. Erdin, T. Huynh, D. Medina, P. Colella, TFEB links autophagy to lysosomal biogenesis, Science (80-.). 332 (2011) 1429–1433.
[72] W.-L. Sun, P.M. Quizon, J. Zhu, Molecular mechanism: ERK signaling, drug addiction, and behavioral effects, in: Prog. Mol. Biol. Transl. Sci., Elsevier, 2016: pp. 1–40.
[73] H. Wang, L. Wu, B.M. Reinhard, Scavenger receptor mediated endocytosis of silver nanoparticles into J774A. 1 macrophages is heterogeneous, ACS Nano. 6 (2012) 7122–7132.
[74] Y. Geng, T. Kodama, G.K. Hansson, Differential expression of scavenger receptor isoforms during monocyte-macrophage differentiation and foam cell formation., Arterioscler. Thromb. a J. Vasc. Biol. 14 (1994) 798–806.
[75] P.J. Gough, D.R. Greaves, H. Suzuki, T. Hakkinen, M.O. Hiltunen, M. Turunen, S.Y. Herttuala, T. Kodama, S. Gordon, Analysis of macrophage scavenger receptor (SR-A) expression in human aortic atherosclerotic lesions, Arterioscler. Thromb. Vasc. Biol. 19 (1999) 461–471.
[76] S. Hironosuke, A. Masanori, H.C. C., W. Daiana, T.W. Robert, L. Peter, L.R. T., Biomechanical Strain Induces Class A Scavenger Receptor Expression in Human Monocyte/Macrophages and THP-1 Cells , Circulation. 104 (2001) 109–114. https://doi.org/10.1161/hc2701.091070.
[77] M. Arredouani, Z. Yang, Y. Ning, G. Qin, R. Soininen, K. Tryggvason, L. Kobzik, The Scavenger Receptor MARCO Is Required for Lung Defense against Pneumococcal Pneumonia and Inhaled Particles , J. Exp. Med. 200 (2004) 267–272. https://doi.org/10.1084/jem.20040731.

Legends to figures.

Figure 1. A) **Representative Cryo-EM images** of nanoARC and B) nanoARC(ALN) [No differences were found with nanoARC-chol and nanoARC-chol(ALN)]; C): representative TEM cut showing J774A1 cells incubated with HSPC-Chol nanoliposomes; D): representative TEM cut showing J774A1 cells incubated with nanoARC. No evidence of multilayered vesicles was observed.
N: nuclei; mitochondria: ⇗ ; membrane surrounded cytoplasmic vesicles: ➚

Figure 2. SPR sensorgrams of serum proteins and PLA2 interaction on adsorbed nanovesicles (nanoARC and nanoliposomes). n=2

Figure 3. ALN release upon nanovesicles dilution. (A) ALN released from nanovesicles after 3 h of dialysis and (B) size and PDI of nanovesicles before and after 3 h of dialysis

Figure 4. **Uptake of nanovesicles by J774A.1 cells**. Normalized RhPE fluorescence intensity of J774A.1 cells upon 1 and 5 h of incubation with RhPE-labeled nanovesicles, alone or pre-incubated with human plasma. Values are expressed as mean ± SD (n=3).

Figure 5. J774A.1 cells viability upon nanovesicles uptake. J774A.1 cell viability upon 24 h (A) and 48 h (B) of incubation with nanovesicles, nanovesicles (ALN) and free ALN. Values are expressed as mean ± SD (n = 3).

Figure 6. **Effect of nanovesicles on J774A.1 cells metabolism**: (A) Induction of acidic vesicles; (B) Mitochondrial membrane potential (red/green (JC-1 aggregate/monomer) ratio); (C) Intracellular ATP content and (D) Mitophagy: representative fluorescence confocal microscopies of J774A.1 cells labelled with Lysotracker Green and Mitotracker Red and incubated with nanovesicles. Magnification: 60 X. Insets: magnified images of 1 cell.

Figure 7. Induction of apoptosis-necrosis on J774A.1 cells. (A) J774A.1 cell death assessment upon 24 h of incubation with nanovesicles. Cells were stained with YO-PRO-1 and PI to detect the levels of early apoptosis and necrosis (n = 3). (B) Representative J774A.1 cells microscopy images after 24 h incubation with 100 µg/ml nanoARC: bright field, Hoechst staining (blue nuclei), YO-PRO staining (green, for apoptotic cells), PI staining (red, for necrotic cells). Magnification 20X.

Figure 8. **Western blot analysis** of AKT/pAKT, ERK/pERK on J774A.1 cells after 24 h incubation with nanoARC or nanoliposomes (n=3). Lipid dose indicated are in µg/ml.

Figure 9. Induction of reactive oxygen species (ROS) and reactive nitrogen species (RNS). (A) Fluorescence intensity of carboxy-DCFDA and (B) amount of RNS produced by J774 A.1 cells after 24 h incubation with nanovesicles in the absence and presence of LPS (1 µg/ml). Identical results were obtained for sequential incubation of nanovesicles and LPS. Values are expressed as means ± SD (n = 3). Asterisks indicate significant differences against LPS or medium control.

Figure 10. *In vitro* anti-inflammatory activity. Proinflammatory cytokines released by J774A.1 cells where measured upon 24 h of coincubation of nanovesicles with 1 µg/ml LPS. Identical results were obtained for sequential incubation of nanovesicles and LPS. Values are expressed as means ± SD (n = 3).

Supplementary Figure 1. (A) Acidic vesicles 24 h after sample washing (B) Forward scattering and (C) Side scattering; (D) Mitochondrial membrane potential 24 h after sample washing.

Supplementary Figure 2. Representative microscopy images of J774A.1 cells after 24 h incubation with 500 µg/ml nanoARC or nanoliposomes HSPC-Chol: **bright field,** Hoechst staining (blue nuclei), YO-PRO staining (green, for apoptotic cells) and PI staining (red, for necrotic cells). Magnification 20X.

Supplementary Figure 3. TUNEL assay. Histograms showing TUNEL-488 nm intensity versus cell count for J774A.1 cells after 24 h incubation with 50, 100 and 500 µg/ml nanoARC or HSPC-chol nanoliposomes.

Supplementary Figure 4. Representative microscopy images of (A) J774A.1 cells stained with Oil Red. (B): J774A.1 cells treated with OxLDL and stained with Oil Red

Supplementary Figure 5. FC viability upon nanovesicles uptake. FC viability upon 24 h (A) and 48 h (B) of incubation with nanovesicles, nanovesicles (ALN) and free ALN. Values are expressed as mean ± SD (n = 3).

Table 1. Structural features of nanovesicles

Formulation	ALN (µg/ml ± SD)	TL (mg/ml ± SD)	ALN /TL (µg/mg ± SD)	EE (%)	Mean diameter (nm ± SD)	PDI	ζ potential (mV ± SD)	GP	FA
nanoARC	-	7.5 ± 1.3	-	-	168.9 ± 11	0.19 ± 0.01	-41.5 ± 4.5	-0.14 ± 0.02	0.22 ± 0.01
nanoARC-chol	-	8.3 ± 1.8	-	-	185.1 ± 11	0.23 ± 0.08	-40.5 ± 5.4	0.28 ± 0.01	0.22 ± 0.02
HSPC-chol	-	7.0 ± 1.7	-	-	276.7 ± 11	0.30 ± 0.08	-5.4 ± 1.4	0.50 ± 0.1	0.26 ± 0.04
nanoARC-ALN	234 ± 88	6.3 ± 1.3	38.4 ± 16.5	1.9 ± 0.8	187 ± 2	0.25 ± 0.05	-40.8 ± 1.2	-0.31 ± 0.03	0.19 ± 0.03
nanoARC-chol-ALN	322 ± 140	6.2 ± 1.1	49.5 ± 23.0	2.6 ± 1.4	234 ± 9	0.31 ± 0.03	-41.5 ± 0.2	0.25 ± 0.03	0.16 ± 0.02
HSPC-chol-ALN	395 ± 146	6.5 ± 1.6	60.1 ± 7.5	3.2 ± 1.0	252 ± 9	0.22 ± 0.06	-4.6 ± 1.8	0.55 ± 0.01	0.22 ± 0.01

Data are expressed as mean ± standard deviation from five independent batches.

ALN: alendronate; EE: encapsulation efficiency; FA: Laurdan fluorescence anisotropy; GP: Laurdan general polarization; PDI: Polydispersity Index; SD: Standard Deviation; TL: total lipids

Table 2. ∆PeakMinAngle values

	∆PeakMinAngle / deg	
	nanoARC	Liposomes
Nanovesicles	0.6 ± 0.14	1.055 ± 0.57
Human plasma	0.15 ± 0.03	0.01 ± 0.01
PLA2	-0.095 ± 0.01	-0.19 ± 0.04

Fig. 1

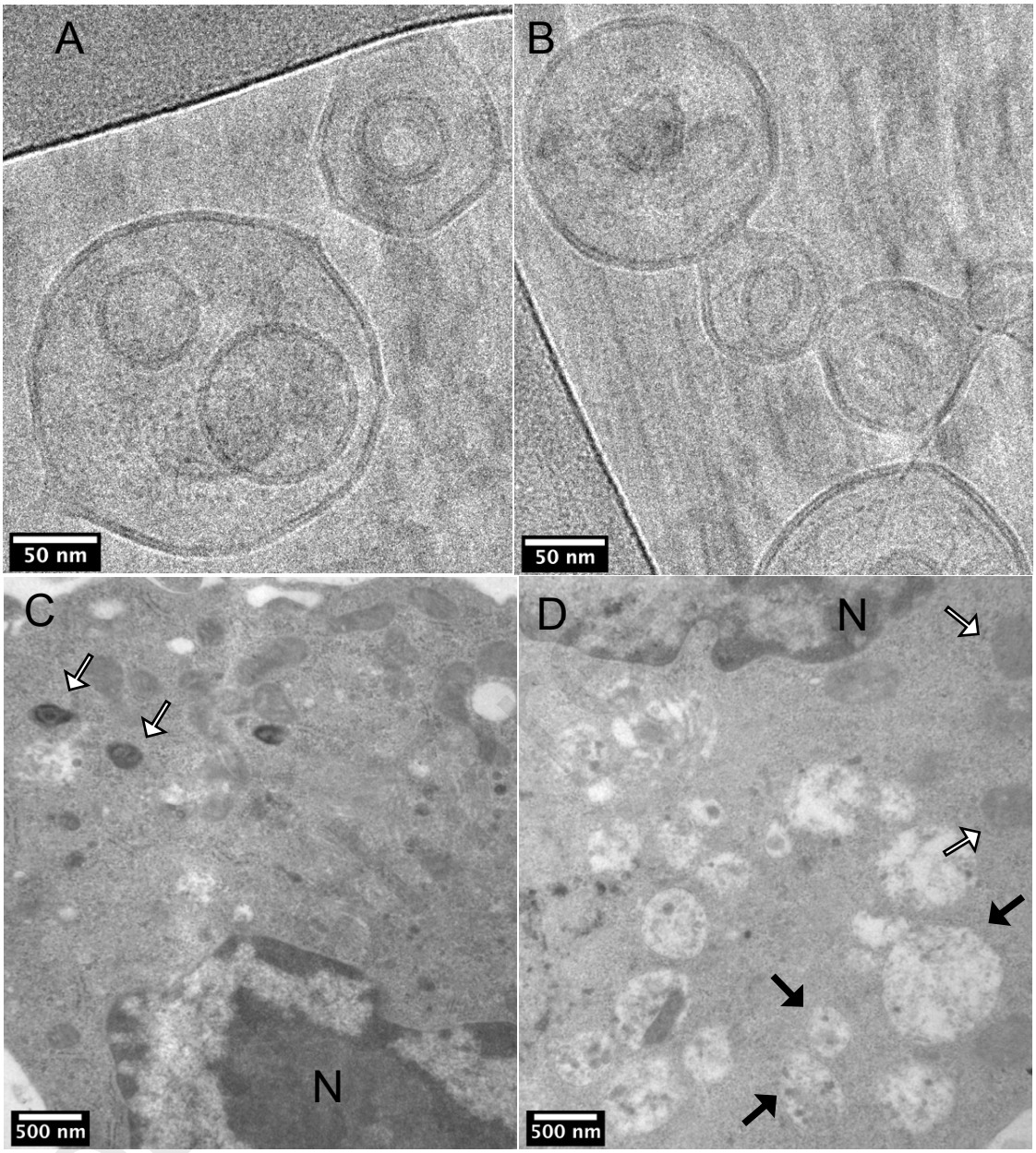

Fig. 2

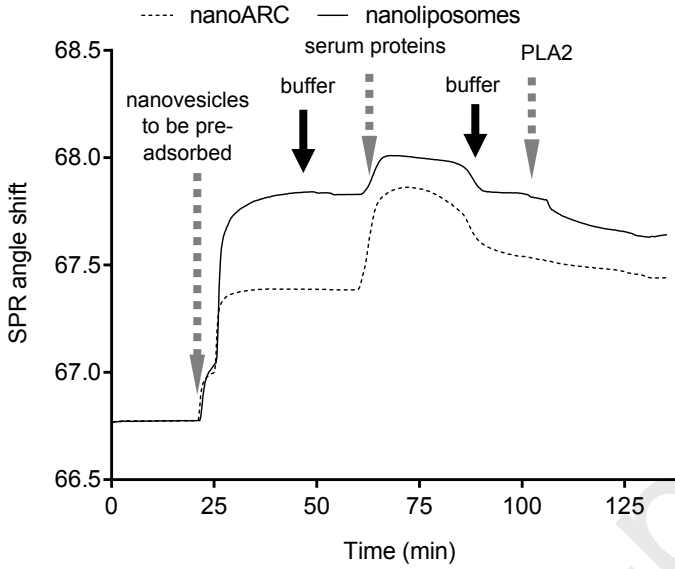

Fig. 3

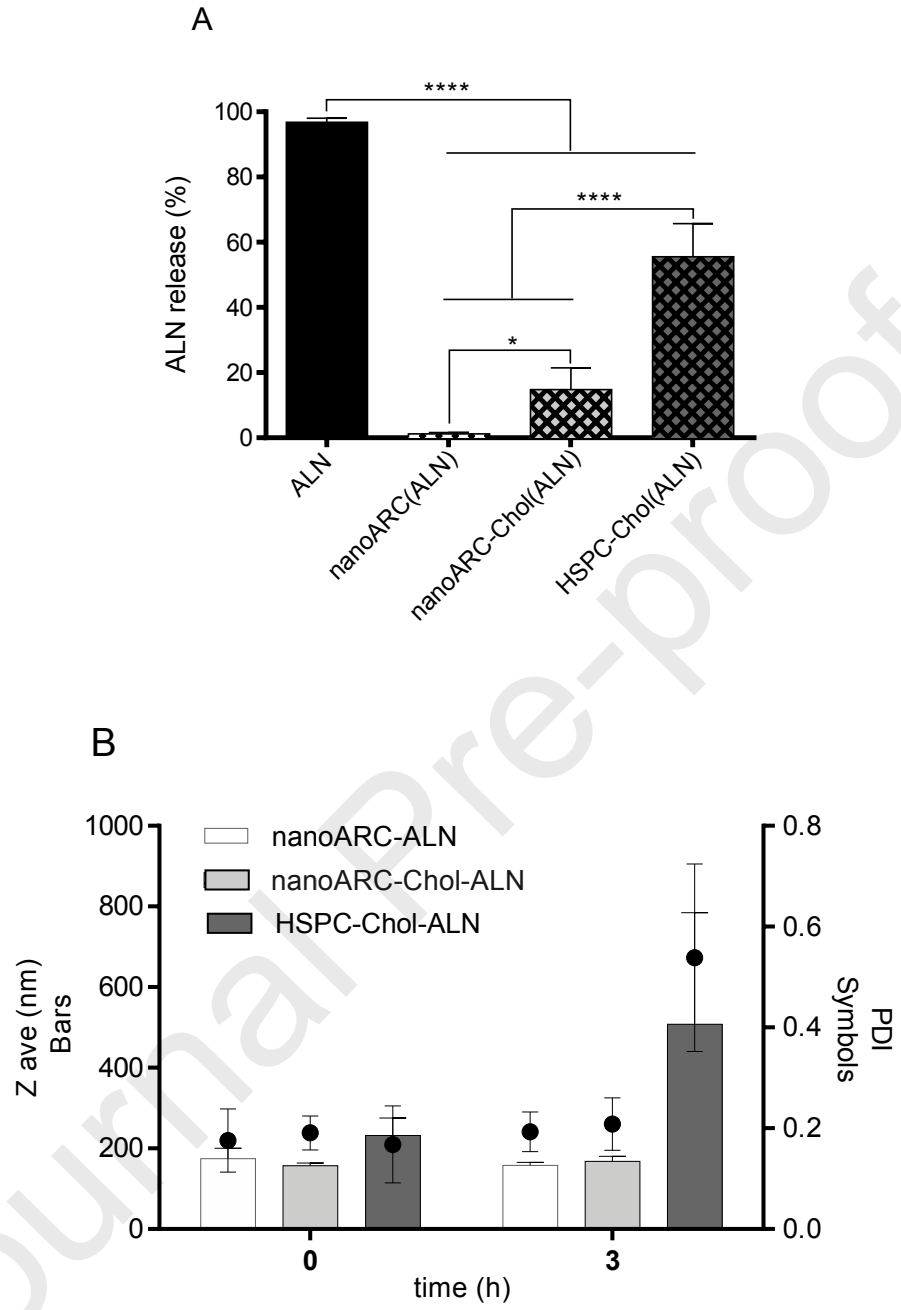

Fig. 4

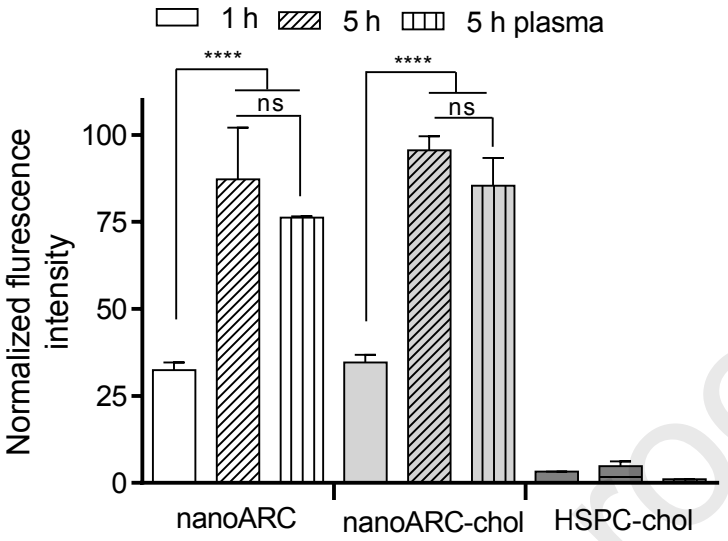

Fig. 5

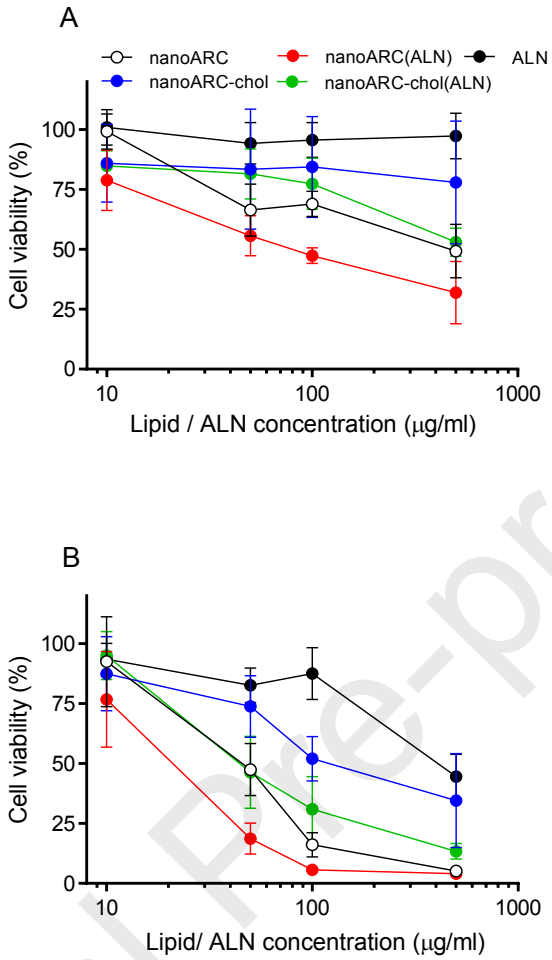

Fig. 6

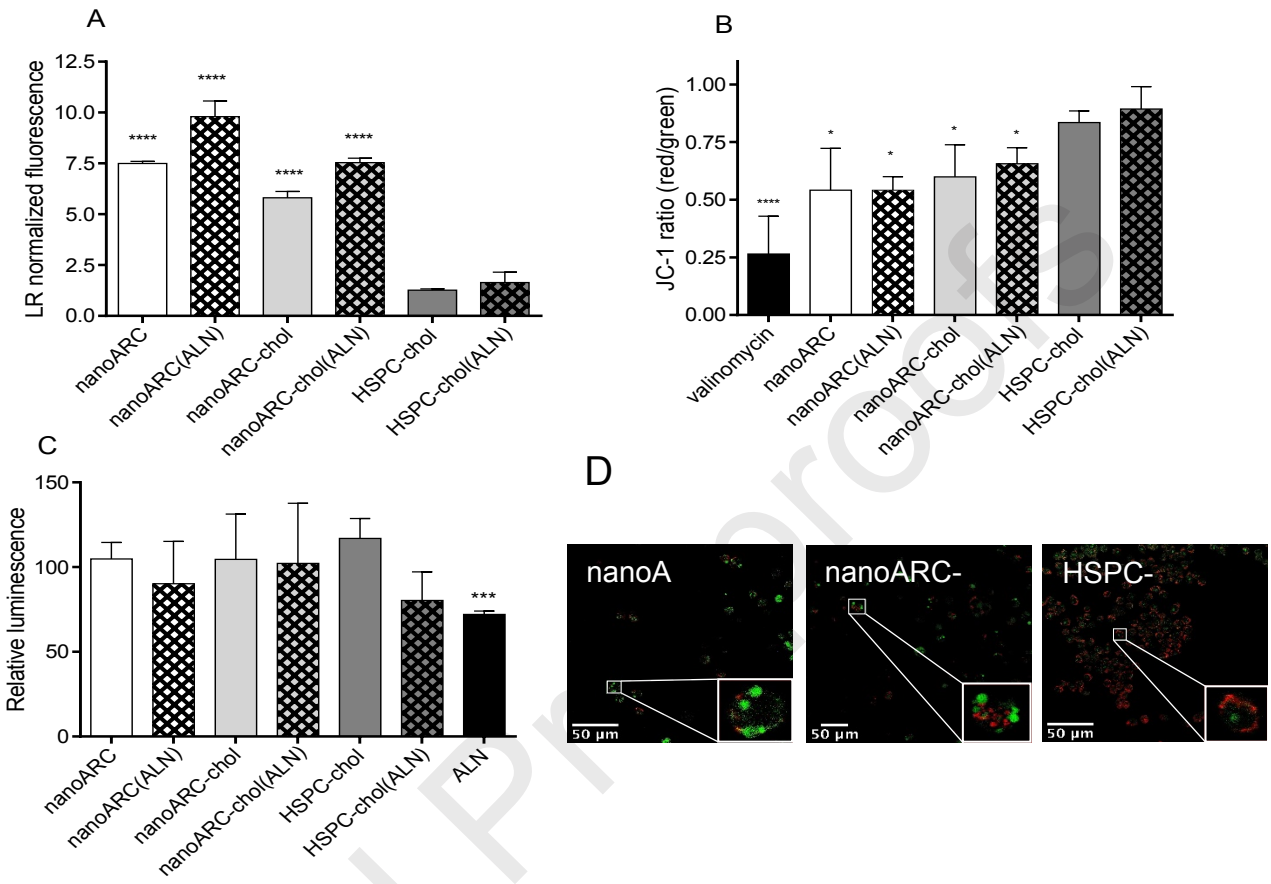

Fig. 7

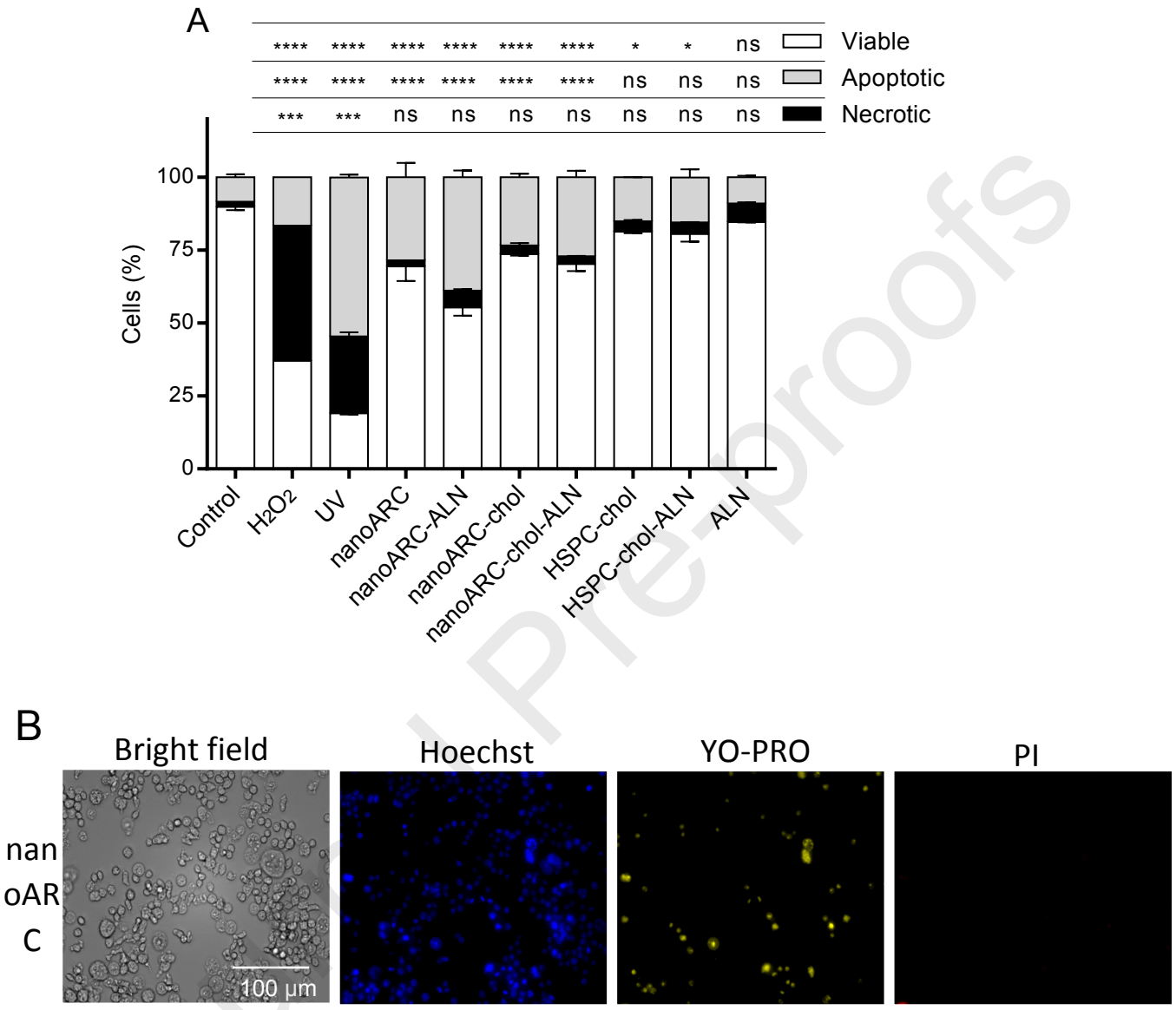

Fig. 8

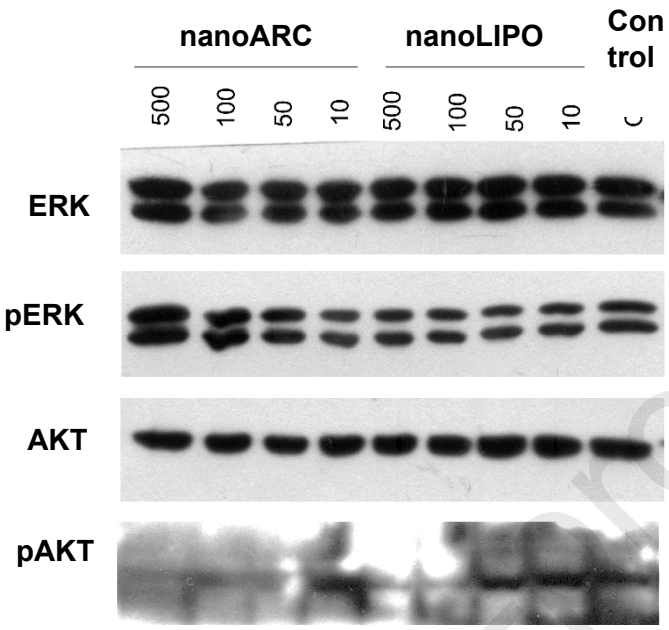

Fig. 9

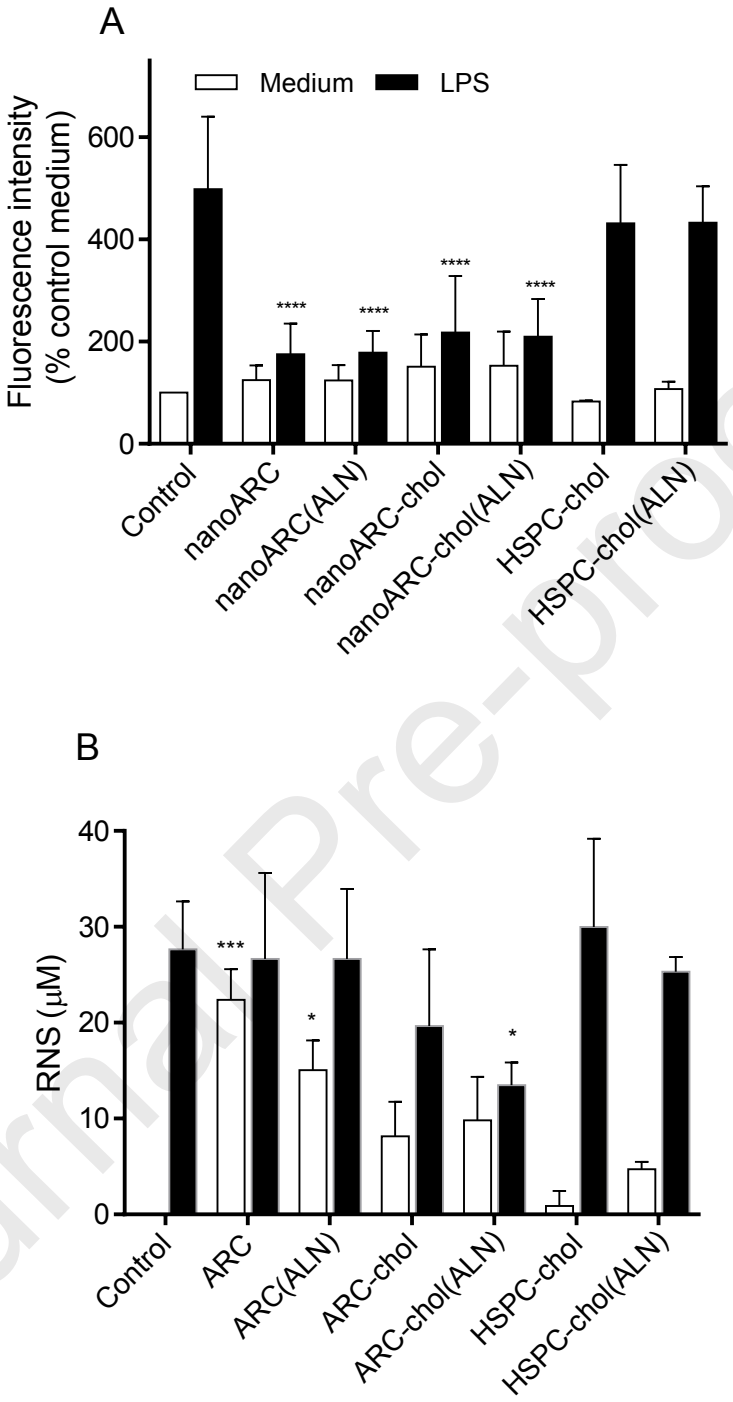

Fig. 10

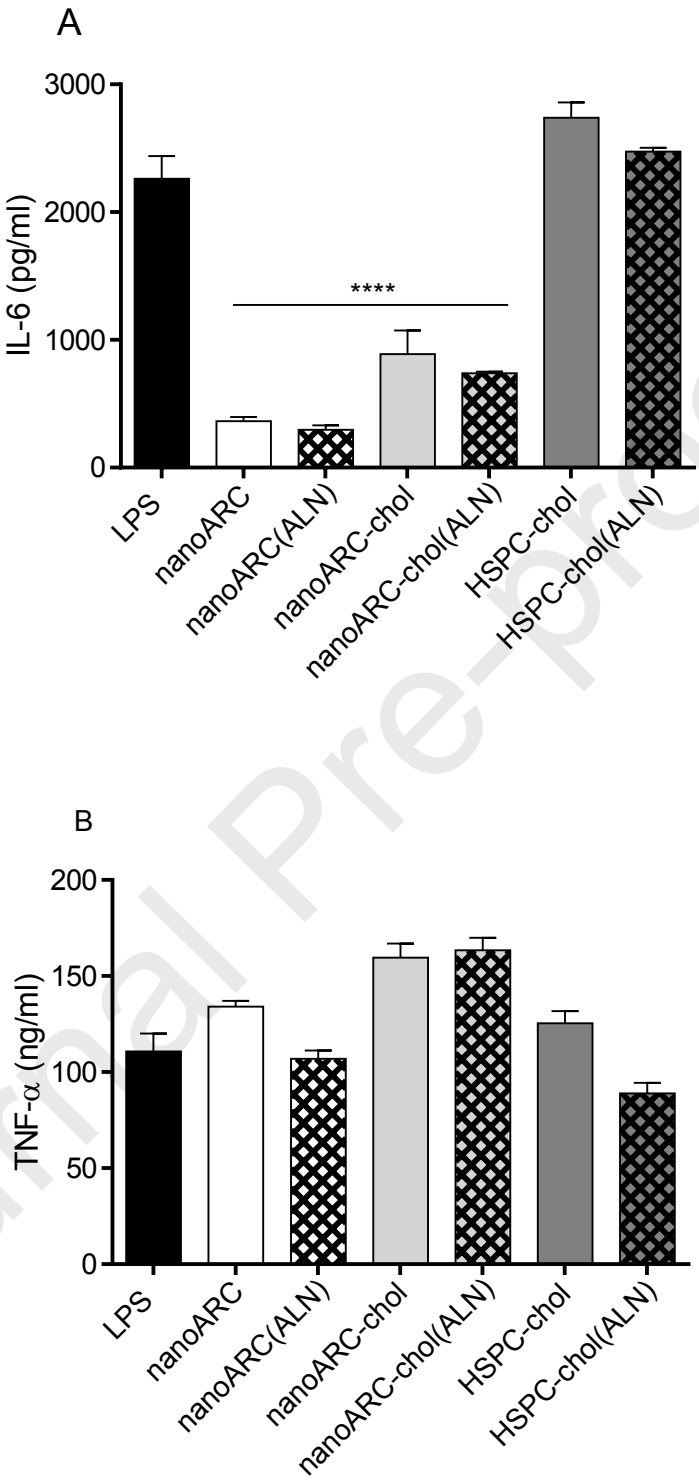

Supplementary Fig 1.

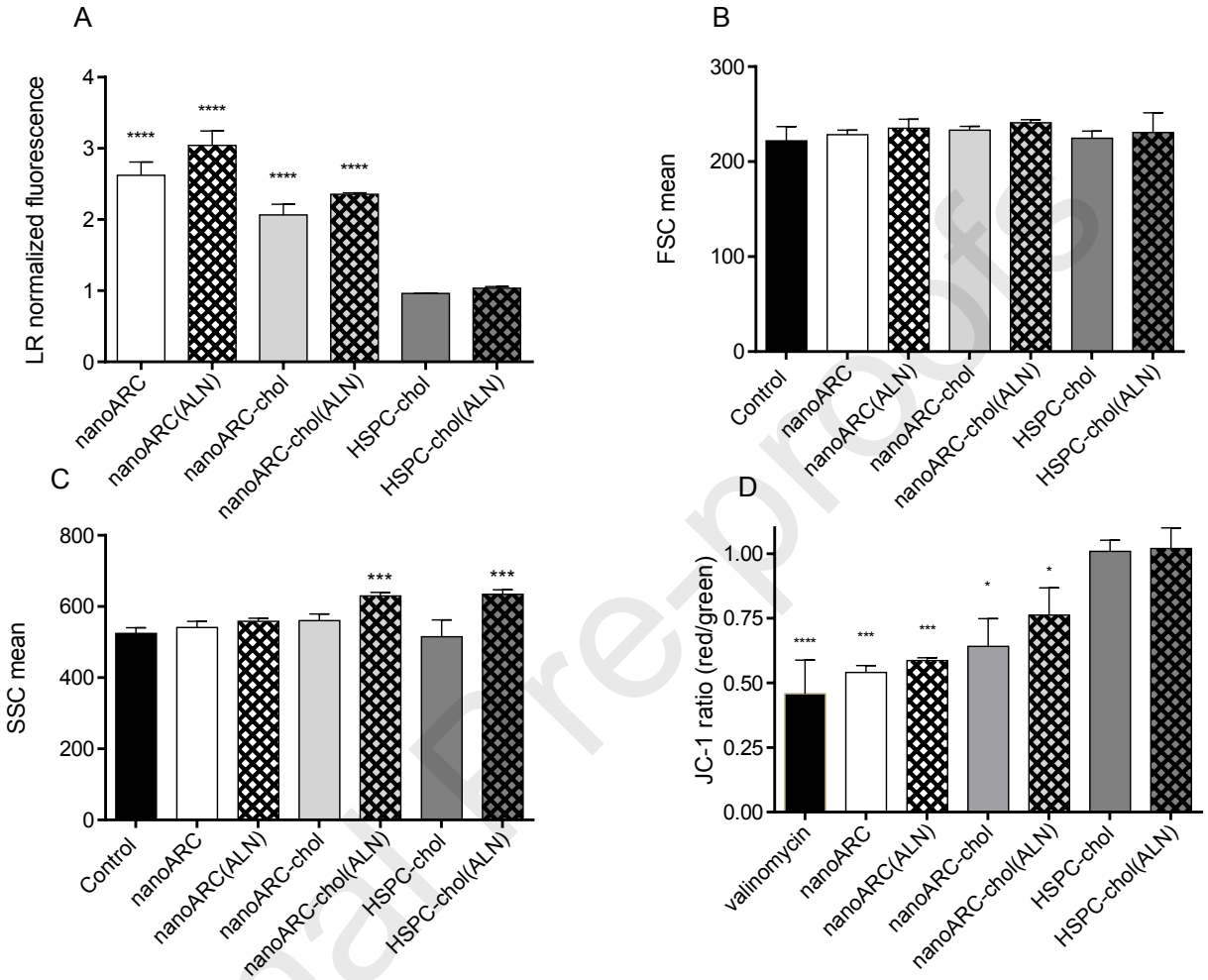

Supplementary Fig 2.

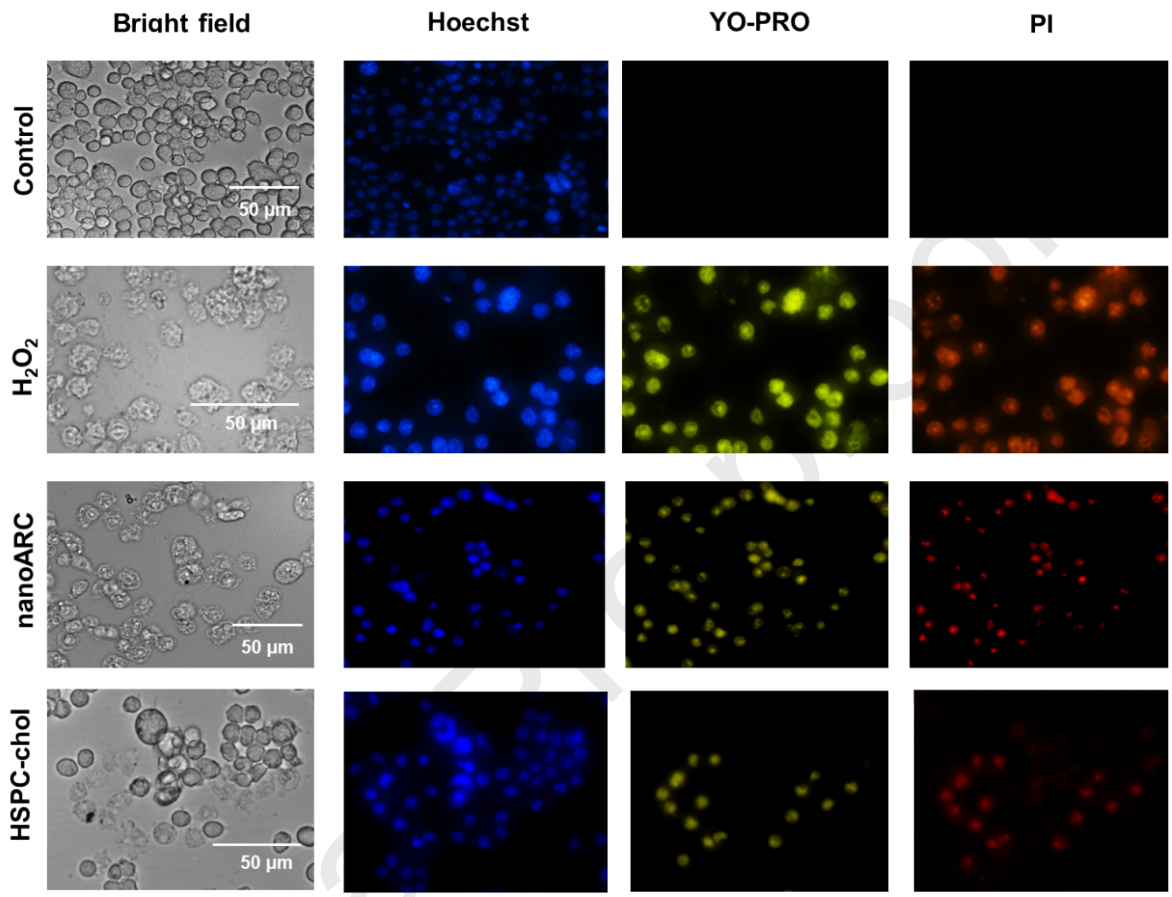

Supplementary Fig 3.

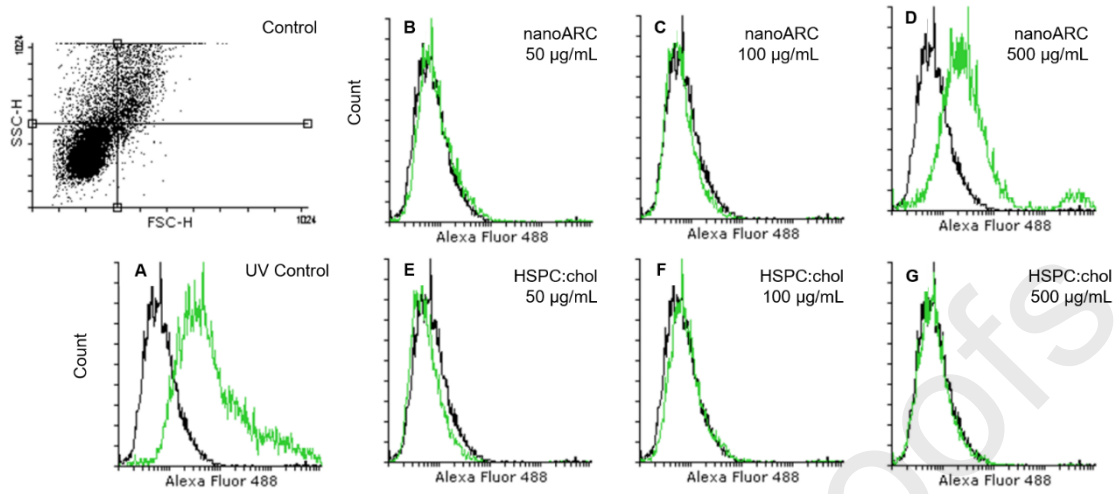

Supplementary Fig 4.

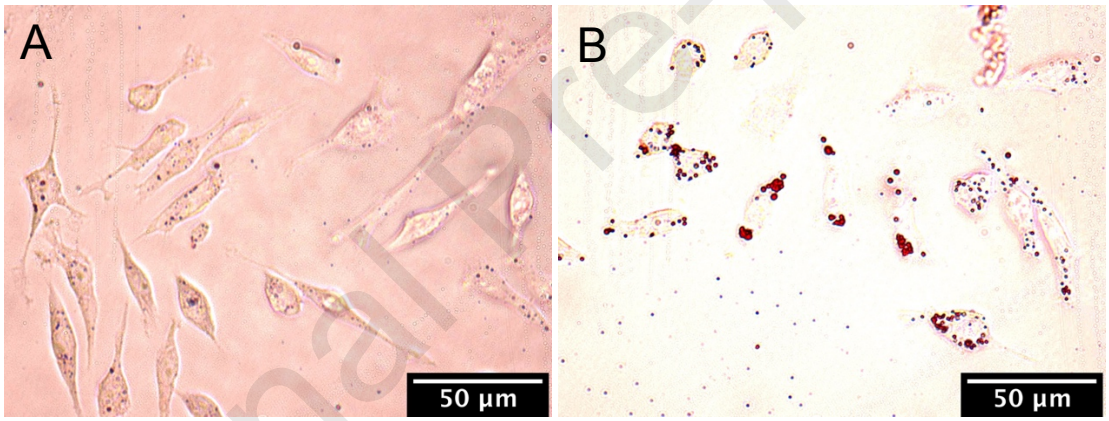

Supplementary Fig 5.

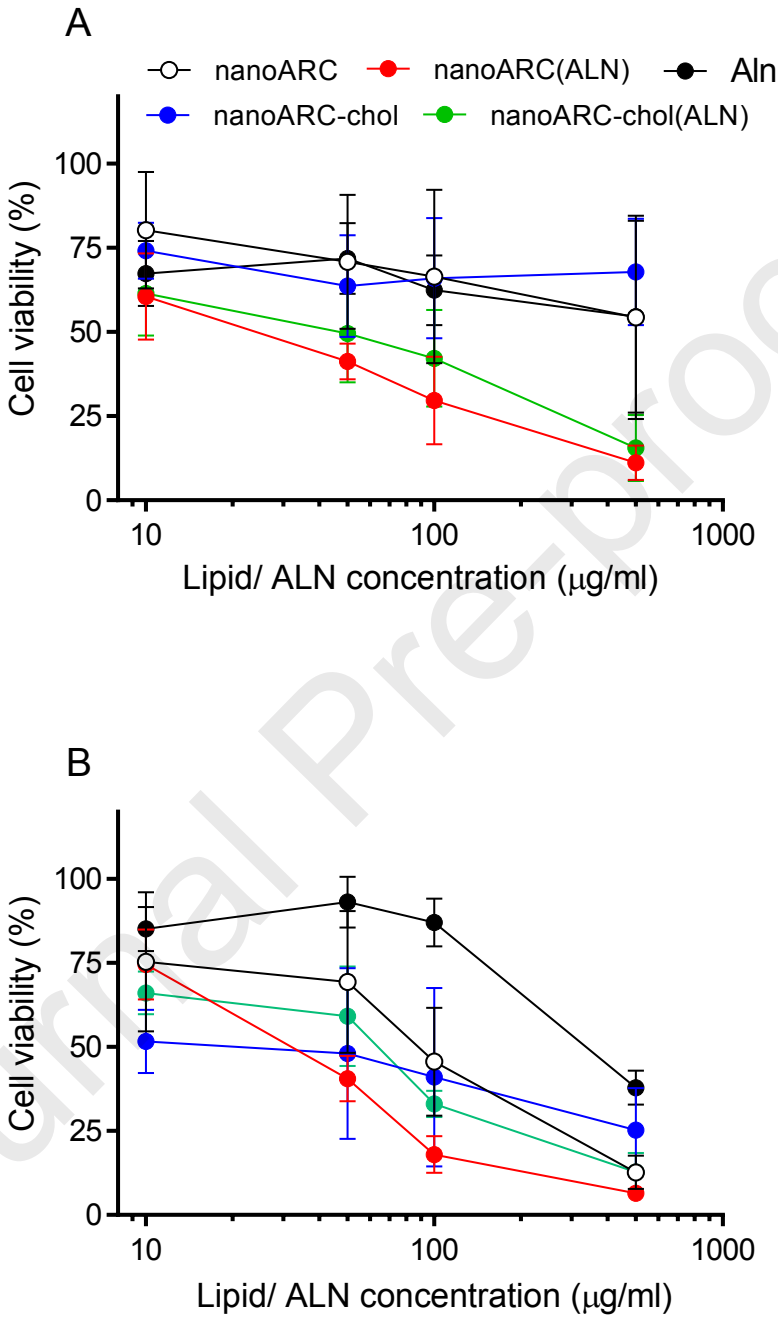

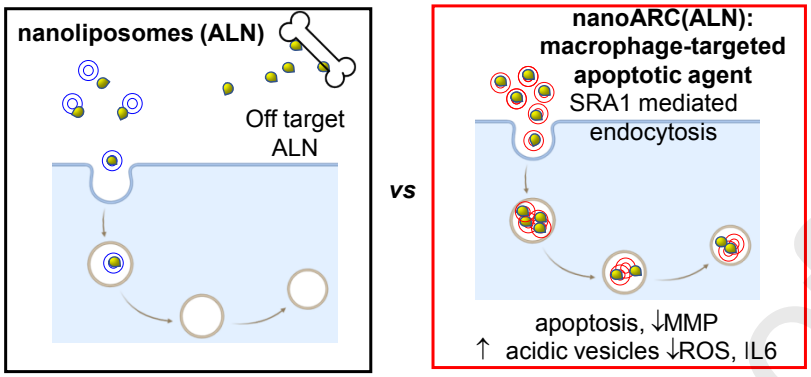

ALN: alendronate; nanoARC: nanoarchaeosomes; SRA1: scavenger receptor Class A1, MMP: mitochondrial membrane potential, ROS: reactive oxygen species